

学位論文（博士）

Thioredoxin-interacting protein is a pivotal factor
for brown adipose tissue function and adaptive
thermogenic property to acute cold stress

(Thioredoxin-interacting protein は褐色脂肪組織の
機能および急性寒冷ストレスへの適応的熱産生特性にお
ける重要な因子である)

氏名 Zou Meng

所属 山口大学大学院医学系研究科

医学専攻 病態制御内科学講座

令和6年11月

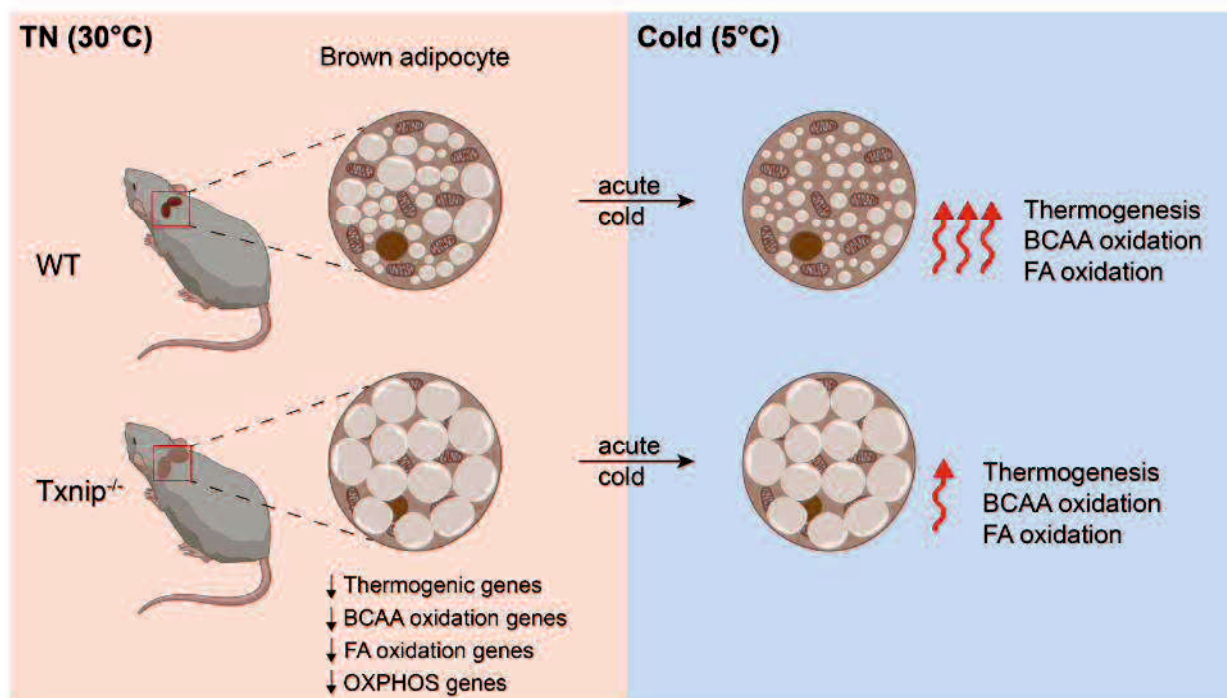
Contents

1. Abstract	1
2. Background	2
3. Aim	3
4. Materials and methods	4
5. Results	11
6. Discussion	25
7. Conclusion	26
8. Acknowledgement	27
9. References	28

1. Abstract

Mammals adaptively regulate energy metabolism in response to environmental changes such as starvation and cold circumstances. Thioredoxin-interacting protein (Txnip), known as a redox regulator, serves as a nutrient sensor regulating energy homeostasis. Txnip is essential for mice to adapt to starvation, but its role in adapting to cold circumstances remains unclear. To investigate thermogenic function in mice lacking Txnip (*Txnip*^{-/-}), indirect calorimetry, biochemical, histological, transcriptomic, and metabolomic analyses were performed in vivo or in dissected brown adipose tissue (BAT) under various temperature conditions. Txnip protein levels in BAT were upregulated by the acute cold exposure. *Txnip*^{-/-} mice acclimated to thermoneutrality (30°C) exhibited significant BAT enlargement and triglyceride accumulation with downregulation of BAT signature and metabolic gene expression. Upon acute cold exposure (5°C), *Txnip*^{-/-} mice showed a rapid decline in BAT surface temperatures with the failure of increasing metabolic respiration, developing lethal hypothermia. The BAT dysfunction and cold susceptibility in *Txnip*^{-/-} mice were corrected by acclimation to 16°C, protecting the mice from life-threatening hypothermia. Transcriptomic and metabolomic analysis on BAT revealed that despite preserving glycolysis, the BAT of *Txnip*^{-/-} mice failed to activate the catabolism of branched-chain amino acids and fatty acids in response to acute cold stress. Thus, our results revealed that Txnip is required for maintaining basal BAT function and ensuring cold-induced thermogenesis.

Graphical abstract



2. Background

Mammals possess sophisticated physiological mechanisms to adapt to challenging environmental conditions, such as prolonged starvation, endurance exercise, and cold circumstances. Regulation of nutrient metabolism to maintain energy homeostasis is essential for these adaptive responses.

2.1 Thioredoxin-interacting protein (Txnip) controls multiple aspects of energy metabolism

Thioredoxin-interacting protein (Txnip) binds to and inhibits thioredoxin, thereby modulating the cellular redox state and promoting oxidative stress(1-4). Structurally, Txnip contains arrestin domains and belongs to the α -arrestin family (Figure 1a). Txnip engages in various redox-independent cellular functions, primarily relying on its role as an ancestral α -arrestin family scaffold(5-8). Given its extensive influence in biological processes, such as redox regulation, cell growth, differentiation, apoptosis, inflammation, and energy metabolism, Txnip serves as a nutrient sensor regulating energy homeostasis across various systems, including the liver, islet β -cells, skeletal muscle, white adipose tissue, and immune cells (Figure 1b and c)(9-18). Specifically, *Txnip*-deficient mice exhibit resistance to diabetes(19) and susceptibility to starvation, alongside attenuated inflammatory response and exercise intolerance(6, 13, 15). These lines of evidence suggest that in mice, Txnip plays a role in adapting to physiological stresses through the regulation of energy metabolism. However, its role in non-shivering thermogenesis, a crucial aspect of energy expenditure in response to cold exposure, remains poorly understood.

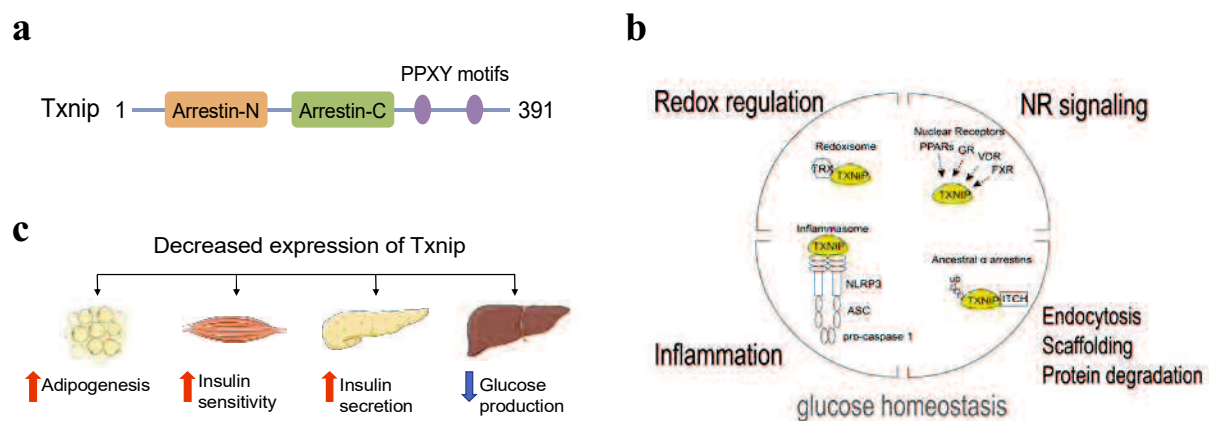


Figure 1. Txnip's involvement in energy metabolism

a) Structural features of Txnip as α -arrestin family protein.

b) Txnip regulates glucose homeostasis through complex biological processes (The figure is modified based on the figure in Reference 18).

c) Txnip regulates adipogenesis in white adipose tissue, insulin sensitivity in skeletal muscle, insulin secretion in pancreatic β cells, and glucose production in the liver.

2.2 Brown adipose tissue (BAT) is a major metabolic and thermogenic site

Non-shivering thermogenesis serves as a fundamental mechanism for maintaining core body temperature and metabolic balance under cold stress. In rodent models, two types of thermogenic adipocytes have been described, each with distinct developmental features (Figure 2a)(20). Classic brown adipocytes are found in BAT depots, whereas beige adipocytes are primarily distributed in subcutaneous white adipose tissue (WAT). Beige adipocytes arise postnatally in response to external stimuli, such as chronic cold exposure, whereas brown adipocytes, once developed, maintain a relatively high thermogenic gene expression, remaining primed for thermogenesis, even without stimulation(21). In response to an adaptive challenge, BAT efficiently oxidizes glucose, lipids, and amino acids to rapidly generate heat through uncoupling protein 1 (Ucp1)-mediated proton gradient uncoupling of mitochondrial respiration (Figure 2b)(22, 23). Despite significant research on the various signaling pathways and metabolic processes of BAT non-shivering thermogenesis(24-28), the precise role of *Txnip* in this context remains unclear.

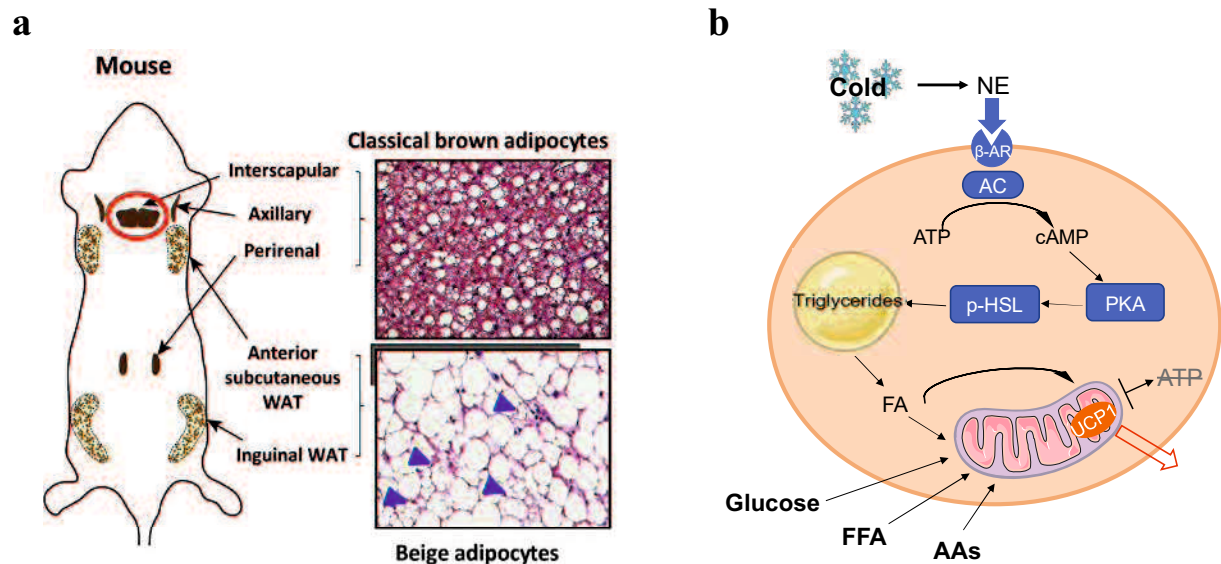


Figure 2. Localization and function of brown adipose tissue in mice

a) Anatomical locations of thermogenic fat in mice and representative images of haematoxylin-eosin (H&E) staining in thermogenic adipocytes (The figure is modified based on the figure in Reference 20).

b) Brown adipocytes dissipate energy from glucose, fatty acids (FAs), and amino acids (AAs) into heat under cold circumstances.

3. Aim

Txnip is essential for mice to adapt to starvation and endurance exercise, but its role in adapting to cold circumstances remains unclear. Hence, this study aimed to explore the effects of *Txnip* deficiency on BAT non-shivering thermogenesis under various temperature conditions using *Txnip*-deficient mice and their BAT.

4. Materials and methods

4.1 Animals

Animal experiments adhered to the ethical regulations and protocols approved by the Institutional Animal Care and Use Committee of Yamaguchi University School of Medicine, Yamaguchi, Japan. Mice were housed in a specific-pathogen-free and climate-controlled facility at 23°C under a 12-h light/dark cycle with standard chow (Oriental yeast, Tokyo, Japan) and water ad libitum. For ketogenic diet (KG) studies, mice were fed either a modified KG or a control diet from 10 weeks of age for 1 week. The diet compositions used in this study are presented in Table 1. For thermoneutrality studies, mice were acclimated to 30°C for 1 week in a climate-controlled animal chamber (Shin Factory, HC-10, Fukuoka, Japan). *Txnip*^{-/-} mice were generated as previously described(29) and maintained on a C57B/6J background, while *Txnip*^{+/-} mice were obtained by crossing C57B/6J with *Txnip*^{-/-} mice. All experiments were performed on male age-matched mice (9–12 weeks old), unless stated otherwise. Mice of identical genotypes were randomly allocated to different treatment groups without blinding.

Table 1: Main composition of the diets used in this study

	Standard chow		Modified Control diet		Modified ketogenic diet	
	g/100g	kcal%	g/100g	kcal%	g/100g	kcal%
Protein	23.1	25	11.9	12	17.9	12
Carbohydrate	55.3	62	73.4	77	9.4	6
Fat	5.1	13	4.4	10	56.7	82
Crude fiber	2.8	0	4.4	0	7.4	0
Moisture and crude ash	13.7	0	5.9	0	8.5	0
Total energy (kcal/100g)	359		381		619	

4.2 Cold tolerance test

For acute cold exposure, mice were acclimated to thermoneutral (TN, 30°C) or room temperature (RT, 23°C) for 1 week before being exposed to cold (5°C) and then individually housed in pre-chilled cages with bedding and free access to water but no food. The core body temperature of the mice was monitored hourly for pre-housing at 30°C or every 2 h for pre-housing at 23°C using a rectal probe (A&D Company, Tokyo, Japan). For chronic cold exposure, mice were acclimated to 16°C for 1 week and then transferred to cold (5°C). A core body temperature of $\leq 10^{\circ}\text{C}$ was considered an event for survival analysis.

4.3 Infrared thermography

Infrared images of the mice were captured using a handheld thermal camera (FLIR E53, Wilsonville, OR, USA). To expose the BAT surface area, a small amount of Vaseline was applied between the shoulder blades of the mice to brush up the neck fur before capturing the

images. The BAT surface temperature was determined using FLIR Tools version 6 (freely available at <https://flir.custhelp.com>).

4.4 Whole-animal O₂ consumption rate and indirect calorimetry

Whole-animal O₂ consumption rate (VO₂) and CO₂ production rate (VCO₂) were measured, and indirect calorimetry was performed using an Oxymax apparatus (Columbus Instruments, Columbus, OH, USA) equipped with a temperature-controlled animal chamber. Ten-week-old mice were initially monitored and maintained at 23°C for 3 days, followed by 30°C for 7 days before exposure to a cold challenge at 5°C. For assessment under chronic cold conditions, mice were monitored and maintained at 23°C for 3 days and then exposed to 16°C for 7 days before the cold challenge at 5°C. For the norepinephrine (NE) challenge, mice acclimated to 30°C for 1 week were intraperitoneally injected with NE (Sigma-Aldrich, St. Louis, MO, USA) at 1 mg/kg body weight and immediately returned to their cages, continuously monitoring VO₂ until the rates declined. The VO₂ measurements were performed every 18 min for each mouse throughout the experiment, with the VO₂ data normalised to body weight. The presented data include measurements from the final day of each condition and the first day of the condition transition. The theoretical value of heat production, denoted as Heat, was calculated using the formula $(3.815 + 1.232 \times \text{RER}) \times \text{VO}_2$.

4.5 Transmission electron microscopy (TEM)

For TEM sample collection, cardiac perfusion was performed under anesthesia with a fixative buffer (2% glutaraldehyde, 2% paraformaldehyde in 0.1 M phosphate buffer). Interscapular BAT was dissected, cut into 1 mm pieces, and fixed in the fixative buffer (2% glutaraldehyde, 2% paraformaldehyde in 0.1 M phosphate buffer) overnight at 4°C. Samples were rinsed in 0.1 M phosphate buffer and postfixed in 2% osmium tetroxide for 3 hours at 4°C. Then, the samples were dehydrated with a series of graded ethanol and embedded in epoxy resin. Ultrathin sections were obtained by ultramicrotome with diamond knives, stained with 2% uranyl acetate and lead citrate, and imaged with a JEOL 1400 Flash electron microscope. For image analysis, mitochondria were manually traced and quantified in the NIH ImageJ software.

4.6 Histological analysis

BAT samples were fixed in 4% paraformaldehyde at 4°C overnight, followed by embedding in paraffin and slicing into 3- μ m sections. These sections were stained with haematoxylin and eosin and visualised and photographed using a Keyence BZ-X710 microscope with the BZ-X Viewer software (Keyence, Osaka, Japan). Lipid droplet sizes within brown adipocytes were quantified using the NIH ImageJ software (freely available at <https://imagej.net/ij/index.html>).

4.7 Quantification of BAT triglyceride content

Triglycerides were extracted from BAT using a modified Folch's method(30). Briefly, BAT homogenisation in cold saline was followed by extraction in 2:1 chloroform-methanol (v/v) solution. The extracted triglycerides were resuspended in 2-propanol and quantified using the

LabAssay Triglyceride Kit (FUJIFILM Wako Pure Chemical Corporation, Osaka, Japan), normalised to the protein content determined using a bicinchoninic acid (BCA) protein assay kit (Thermo Fischer Scientific, Waltham, MA).

4.8 Western blot analysis

Tissues were homogenised in radioimmunoprecipitation assay (RIPA) buffer supplemented with protease and phosphatase inhibitor cocktails (Sigma Aldrich, St. Louis, MO, USA) using the gentleMACs Dissociator System (Miltenyi Biotec, Cologne, Germany), followed by centrifugation at $17\,000 \times g$ for 15 min at 4°C. The protein concentration was determined using a BCA protein assay kit (Thermo Fischer Scientific). The protein extracts were diluted in sodium dodecyl sulphate (SDS) sample buffer, denatured by heating (95°C, 3 min), resolved on 4–20% gradient polyacrylamide gels (Cosmo Bio, Tokyo, Japan), and transferred onto nitrocellulose membranes (GE Healthcare, Buckinghamshire, UK). Membranes were blocked using Blocking One (Nacalai Tesque, Kyoto, Japan), followed by overnight incubation with specific primary antibodies at 4°C. The primary antibodies used are listed in Table 2. Specific proteins were visualised on a film using horseradish peroxidase-conjugated anti-mouse IgG or anti-rabbit IgG secondary antibodies (Jackson ImmunoResearch, West Grove, PA, USA), along with an enhanced chemiluminescence substrate kit (GE Healthcare, Chicago, IL, USA). Band intensities were quantified using the NIH Image J software, with α -tubulin or HSP90 bands for loading normalisation. For the detection of phosphorylated HSL (pHSL) in BAT, β_3 agonist CL316243 (Sigma-Aldrich) was intraperitoneally injected into mice at 1 mg/kg body weight.

Table 2. List of antibodies used in this study

Protein	Dilution	Host, MW (kDa)	Antibody cat. no
TXNIP	1:1000	Rabbit mAb, 50	ab188865, Abcam
α -Tubulin	1:5000	Mouse mAb, 52	#3873, Cell Signaling Technology
p-HSL (Ser660)	1:1000	Rabbit pAb, 81, 83	#45804, Cell Signaling Technology
HSL	1:10,000	Rabbit mAb, 81, 83	#18381, Cell Signaling Technology
PPAR γ	1:1000	Rabbit mAb, 53, 57	#2443, Cell Signaling Technology
PGC1 α	1:1000	Rabbit pAb, 100	AB3242, Sigma-Aldrich
UCP1	1:10,000	Rabbit mAb, 33	ab209483, Abcam
HSP90	1:1000	Rabbit pAb, 90	#4874, Cell Signaling Technology
H3K27ac	1:100	Rabbit mAb, 17	#8173, Cell Signaling Technology

p-, phosphorylated; pAb, polyclonal antibody; mAb, monoclonal antibody.

4.9 RNA extraction and gene expression analysis (RT-qPCR)

Total RNA was extracted from BAT and WAT using the TRIzol reagent and Direct-zol RNA

Miniprep Plus Kit (Zymo Research, Irvine, CA, USA) according to the manufacturer's instructions. One microgram of total RNA was used to synthesise cDNA using the High-Capacity cDNA Reverse-Transcription Kit (Applied Biosystems, Waltham, MA, USA). Subsequently, cDNA levels were analysed via quantitative polymerase chain reaction (qPCR) using the Power SYBR Green Master Mix in an ABI Step-One-Plus Real-Time PCR System (Applied Biosystems). Gene expression levels were quantified using the standard curve method ($\Delta\Delta C_t$) and normalized to mouse cyclophilin A expression. All primer sequences are listed in Table 3.

Table 3. List of primers used for real-time qPCR

Gene	Forward Primer 5'-3'	Reverse Primer 5'-3'
<i>Cyclophilin A</i>	TGTGCCAGGGTGGTGA CTTTAC	TGGGAACCGTTTGTGTTTGG
<i>Ucp1</i>	TCAGGATTGGCCTCTACGAC	TGCCACACCTCCAGTCATTA
<i>Pgc1a</i>	CCCTGCCATTGTTAAGACC	TGCTGCTGTTCCTGTTTTTC
<i>mtND1</i>	GTGGCTCATCTACTCCACTGA	TCGAGCGATCCATAACAATAA
<i>HK2</i>	CCAGGGCTGTAGGAACATGG	ACAGATAGCAAGCAGCCTCG

4.10 Quantification of mtDNA copy number

Mitochondrial and nuclear DNA were purified from the BAT of 12-week-old mice using the QIAamp DNA Mini Kit (Qiagen, Hilden, Germany), following the manufacturer's protocols. The DNA concentration and purity were measured using a NanoDrop spectrophotometer (Thermo Fischer Scientific). The DNA samples, diluted to 10 ng/ μ L with UltraPure water (Invitrogen, Camarillo, CA, USA), were analysed by qPCR using a standard curve method to quantify the mtDNA abundance normalised to nuclear genomic DNA abundance. Specifically, mtDNA was quantified using primers targeting the NADH-ubiquinone oxidoreductase chain 1 (*ND1*) gene, while nuclear DNA was quantified using primers targeting the hexokinase 2 (*HK2*) gene. The primer sequences for *ND1* and *HK2* are listed in Table 3.

4.11 BAT NE turnover

BAT NE turnover was determined by measuring the decline in tissue NE content after inhibiting catecholamine synthesis and subsequent re-accumulation through treatment with α -methyl-D, L-p-tyrosine (α -MPT) (Santa Cruz Biotechnology, Inc, Dallas, TX)(31). Mice housed at 23°C were injected with α -MPT (200 mg/kg, i.p.) at 10 am before being exposed to cold at 5°C. After 0 and 3 h of cold exposure, the mice were euthanized via cervical dislocation. BAT was rapidly removed, weighed, snap-frozen in liquid nitrogen, and stored at -80°C. The NE content in the dissected BAT was determined using the Noradrenaline Research ELISA Kit (ImmuSmol, Bordeaux, France) following the manufacturer's instructions.

4.12 Determination of serum BCAA and blood glucose levels

Blood samples from tail veins were used to determine blood glucose levels using an automatic

blood glucometer (Antsense Duo, Horiba, Kyoto, Japan). Serum was obtained by centrifuging the blood samples at $1200 \times g$, 4°C for 10 min. The serum BCAA concentration was determined using the Branched-Chain Amino Acid Assay Kit (Abcam, Cambridge, UK) according to the manufacturer's protocol.

4.13 RNA-seq and analysis

Interscapular BAT RNA was isolated from 10-week-old WT and *Txnip*^{-/-} mice acclimated to either 30°C or 23°C for 1 week, with triplicates for each group. RNA purity and integrity were confirmed using a bioanalyzer (Agilent Technologies, Santa Clara, CA, USA). RNA-seq libraries were generated from 500 ng of total RNA using Poly-A selection, and the NEBNext RNA Library Prep Kit (NEB, Ipswich, MA, USA), according to a standard Illumina protocol. The libraries were quantified using both an Agilent bioanalyzer and qPCR-based quantification (NEB). Sequencing was conducted with single-end 75-bp read length on an Illumina NextSeq 550 instrument, ensuring a depth of at least 20 million reads. The reads were aligned to the University of California Santa Cruz (UCSC) mm10 reference genome using STAR version 2.7.5a(32). Measuring gene expression involved using the “-count exons” command in Homer(33). Subsequent differential gene expression analysis was performed using DESeq2 version 1.8.2(34). Genes exhibiting a fold change >1.25 or <0.8 and an adjusted P value <0.05 were selected as the differentially expressed genes and visualised in a volcano plot. Gene Ontology analysis was performed using Metascape 3.5, and a heat map was constructed to visualise downregulated genes. Genome browser images were captured via IGV 2.16.0v, generating a representative track for each condition from the replicate tag data format files.

4.14 ChIP-seq and analysis

BAT pads were minced in ice-cold PBS and dissociated into single-cell suspensions using the Adipose Tissue Dissociation Kit (Miltenyi Biotec). The resulting cell pellets were fixed first in DSG (disuccinimidyl glutarate) for 30 min and then in 1% formaldehyde for 10 min at RT. Subsequently, cross-linking in cell pellets was quenched by adding 125 mM glycine for 5 min at RT, followed by washing twice with ice-cold $1 \times$ PBS. The resulting cross-linked cell pellets were resuspended in ice-cold Shearing Buffer (50 mM Tris pH 8.0, 10 mM EDTA pH 8.0, 1% SDS, and protease inhibitor) and sonicated using a Biorupter (UCD300, Cosmo Bio, Tokyo, Japan) for six cycles of 30 s on and 30 s off. The sonicated chromatin lysates were diluted tenfold with Dilution Buffer (16.7 mM Tris pH 8.0, 1 mM EDTA pH 8.0, 167 mM NaCl, 1.1% Triton X-100, 0.01% SDS, and protease inhibitor). A portion was set aside for input DNA, while the remainder was incubated with the antibody against H3K27ac (CST#8173) at 4°C overnight. The next day, the chromatin was immunoprecipitated with IgG paramagnetic beads (Invitrogen) at 4°C with rotation for 6 h, and the collected beads were washed six times with Cell Wash Buffer (50 mM Tris pH 7.5, 5 mM EDTA pH 7.5, 150 mM NaCl, 0.5% NP-40), followed by two washes with cold TE buffer (10 mM Tris [pH 8.0] and 1 mM EDTA). Chromatin immune complexes were eluted twice in Bead Elution Buffer (0.1 M NaHCO_3 and 1% SDS) at RT with rotation for 15 min and then de-crosslinked overnight in 0.2 M NaCl at

65°C. The associated proteins were digested with proteinase K at 45°C for 2 h, and the final DNA was purified using the MinElute PCR Purification Kit (Qiagen, Hilden, Germany). ChIP-seq libraries were prepared using the NEBNext Ultra II DNA Library Prep Kit (NEB), and evaluated for their quality and quantity using a combination of Agilent bioanalyzer and DNA High Sensitivity chips (Agilent Technologies). Two biological ChIP replicates were pooled for sequencing on an Illumina NextSeq 550 system, employing a single-end 75-bp read length. The sequencing reads were aligned to the UCSC mm10 reference genome using Bowtie2 version 2.2.6(35). ChIP-seq peak calling and annotation were performed using the Homer(33) program. A motif enrichment analysis was conducted using the ‘findMotifsGenome’ command in Homer within a 200-bp window with default options.

4.15 Metabolomic analysis

The BAT pads were homogenised in acetonitrile/Milli-Q water containing internal standards (H3304-1002, Human Metabolome Technologies, Inc., Yamagata, Japan) using zirconia beads (5 and 3 mm ϕ) and a Micro Smash bead shaker (TOMY SEIKO, Tokyo, Japan). After centrifugation at 2300 \times g, 4°C for 5 min, the upper aqueous layer of the homogenate was filtered through a Millipore 5-kDa cutoff filter at 9100 \times g, 4°C for 120 min to remove macromolecules. The resulting filtrate was vacuum-dried and reconstituted in 50 μ L of Milli-Q water for metabolome analysis.

Metabolome analysis was conducted using capillary electrophoresis time-of-flight mass spectrometry (CE-TOF-MS) for cation analysis and CE-tandem mass spectrometry (CE-MS/MS) for anion analysis following established protocols(36, 37). Briefly, the CE-TOF-MS and CE-MS/MS analyses were performed using an Agilent CE system equipped with an Agilent 6210 TOF mass spectrometer (Agilent Technologies) and an Agilent 6460 Triple Quadrupole LC/MS (Agilent Technologies), respectively. Both systems were controlled by the Agilent G2201AA ChemStation software version B.03.01 for CE (Agilent Technologies), connected via a fused silica capillary (50 μ m i.d. \times 80 cm total length) with commercial electrophoresis buffers (H3301-1001 and I3302-1023 for cation and anion analyses, respectively; Human Metabolome Technologies Inc. [HMT], Yamagata, Japan) serving as the electrolyte. The TOF mass spectrometer scanned from m/z 50 to 1000(36), while the triple quadrupole mass spectrometer operated in the dynamic multiple reaction monitoring (MRM) mode for compound detection. Peaks were extracted using MasterHands, an automatic integration software (Keio University, Yamagata, Japan)(38), and MassHunter Quantitative Analysis B.04.00 (Agilent Technologies) to obtain peak information, including m/z, peak area, and migration time (MT). Signal peaks were annotated according to HMT’s metabolite database based on their m/z values and MTs. Metabolite concentrations were determined via normalisation to internal standards and evaluated using standard curves with three-point calibrations for each standard compound. A principal component analysis (PCA) was performed using HMT's proprietary and R programs(39). Detected metabolites were plotted on metabolic pathway maps using the VANTED software(40).

4.16 Statistical analyses

Data are presented as mean \pm SD unless otherwise stated. GraphPad Prism 9 was used for graphing and statistical analyses. We used unpaired two-tailed Student's t-test for two-group comparisons and one-way or two-way ANOVA for multiple-group comparisons, followed by Bonferroni's post-hoc test. Survival analysis was performed using the log-rank (Mantel–Cox) test. Further details of all statistical analyses are provided in the figure legends, and statistical significance was determined at $P < 0.05$.

5. Results

5.1 *Txnip* insufficiency alters BAT morphology

To investigate the effect of *Txnip* deficiency on BAT physiology, we examined BAT morphology in *Txnip*^{-/-} and *Txnip*-haploinsufficient (*Txnip*^{+/-}) mice. The BAT from *Txnip*^{-/-} mice appeared paler and larger compared to other genotypes (Figure 3a, b), particularly evident under thermoneutral (TN, 30°C) conditions (Figure 3c, d). Microscopically, brown adipocytes of *Txnip*^{-/-} mice exhibited unilocular hypertrophic lipid droplets, a characteristic that intensified upon TN acclimation (Figure 3e, f). *Txnip*^{+/-} mice exhibited similar changes in their brown adipocyte lipid droplets under TN conditions. Correspondingly, the triglyceride content in BAT of *Txnip*^{-/-} mice significantly exceeded that in wild-type (WT) BAT (Figure 3g).

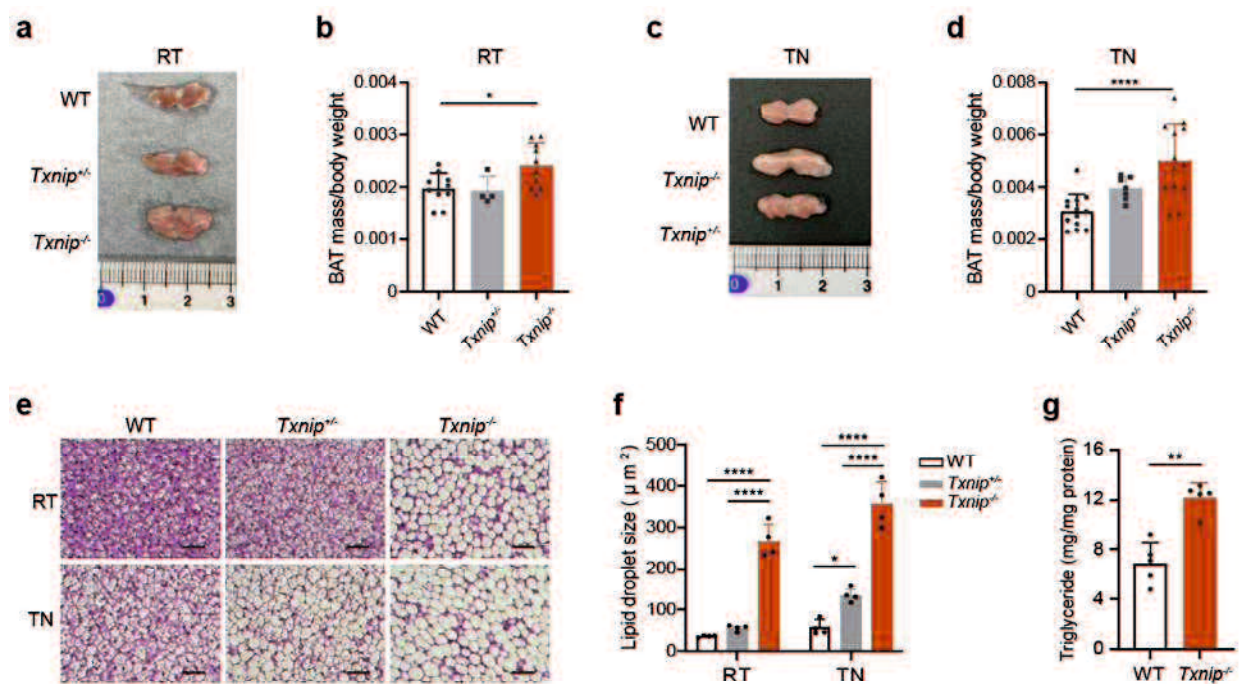


Figure 3. *Txnip* insufficiency alters BAT morphology.

a Representative image of interscapular BAT from 10-week-old wild-type (WT), *Txnip*-haploinsufficient (*Txnip*^{+/-}), and *Txnip*-deficient (*Txnip*^{-/-}) mice housed at room temperature (RT, 23°C);

b Interscapular BAT mass normalized by body weight in 10-week-old WT, *Txnip*^{+/-}, and *Txnip*^{-/-} mice housed at RT on a chow diet (n=10,4,10);

c Representative image of interscapular BAT from 10-week-old WT, *Txnip*^{+/-}, and *Txnip*^{-/-} mice acclimated to thermoneutral (TN, 30°C) conditions for 1 week;

d Interscapular BAT mass normalized by body weight in 10-week-old WT, *Txnip*^{+/-}, and *Txnip*^{-/-} mice acclimated to TN conditions on a chow diet (n=13,7,13);

e Hematoxylin-eosin (H&E) staining of interscapular BAT from 10-week-old WT, *Txnip*^{+/-}, and *Txnip*^{-/-} mice housed at RT and TN conditions. Scale bar is 50 µm;

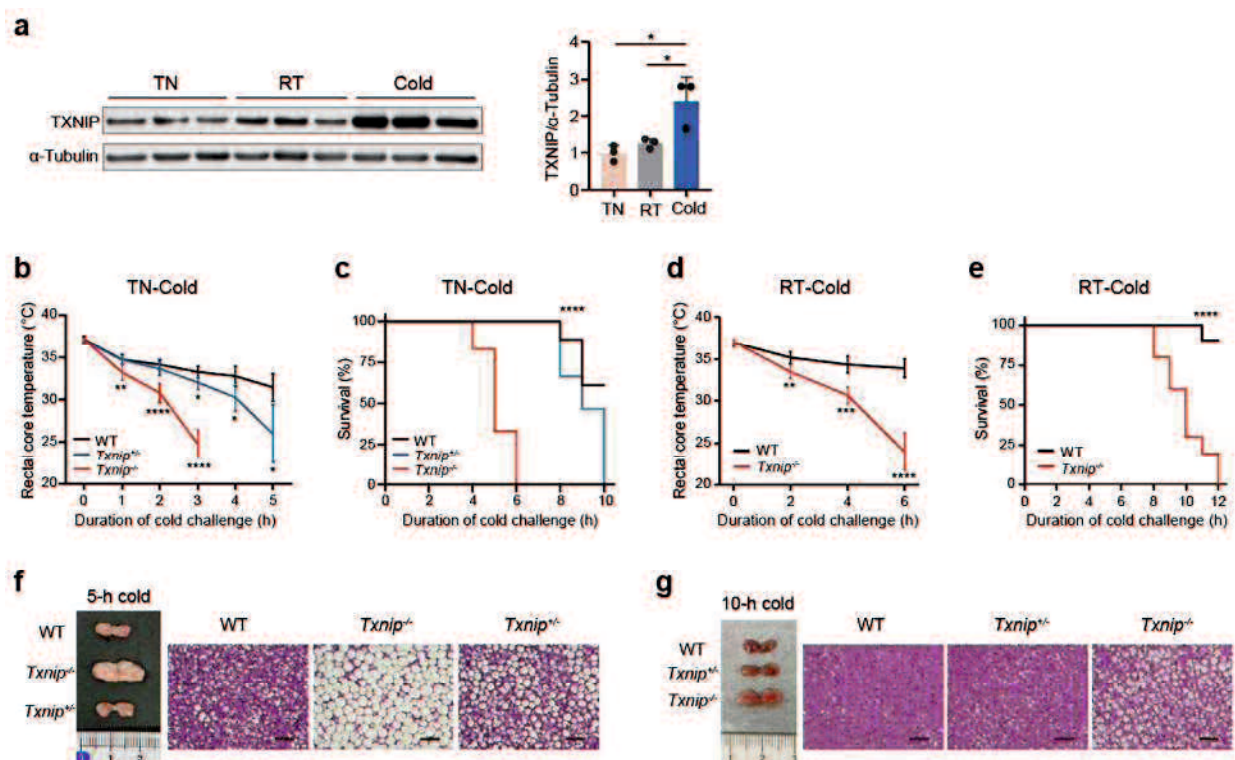
f Quantification of lipid droplet size from BAT H&E-stained slides (n=4);

g Quantification of triglyceride content in the BAT of WT and *Txnip*^{-/-} mice acclimated to TN conditions for 1 week (n=5);

Data: Mean ± SD. Statistical analysis: one-way ANOVA with Bonferroni's post hoc test (**b, d, f**), unpaired Student's t-test (**g**). *p < 0.05, **p < 0.01, ***p < 0.001, and ****p < 0.0001.

5.2 *Txnip* deficiency causes lethal hypothermia under acute cold stress with a lack of BAT thermogenic response

To explore the effect of *Txnip* deficiency on BAT function, we determined the effects of acute cold stress on *Txnip* expression in the BAT of WT mice housed at room temperature (RT, 23°C). Acute exposure to cold conditions (5°C, for 6 h) resulted in a 2-fold increase in *Txnip* protein abundance relative to the baseline (Figure 4a). Subsequent investigation into the impact of reduced *Txnip* levels on cold tolerance showed that both *Txnip*^{-/-} and *Txnip*^{+/-} mice, acclimated to TN conditions before acute cold exposure, exhibited a rapid decline in rectal temperatures, reaching life-threatening hypothermia at 3 h and 5 h, respectively (Figure 4b). *Txnip*^{-/-} mice died within 4–6 h, while *Txnip*^{+/-} mice perished within 8–10 h of cold exposure, indicating a correlation between reduced *Txnip* copy number and deteriorated cold tolerance (Figure 4c). Despite improved survival rates in WT mice housed at RT before cold exposure, *Txnip*^{-/-} mice could not be rescued, perishing within 12 h of cold exposure (Figure 4d and e). Furthermore, following a 5 h cold exposure, BAT from *Txnip*^{-/-} mice retained its enlarged and whitened appearance with most adipocytes exhibiting hypertrophic unilocular lipid droplets, whereas *Txnip*^{+/-} and WT BAT became smaller and brown appearance with varying degrees of multilocular lipid droplets (Figure 4f). This observation was pronounced in mice acclimated to TN conditions but remained consistent in those maintained at RT (Figure 4g). Functionally, thermographic imaging revealed a progressive decline in BAT surface temperatures in *Txnip*^{-/-} mice during acute cold exposure, suggesting that BAT of *Txnip*^{-/-} mice lacks the capability to generate heat in response to acute cold stress (Figure 4h-k).



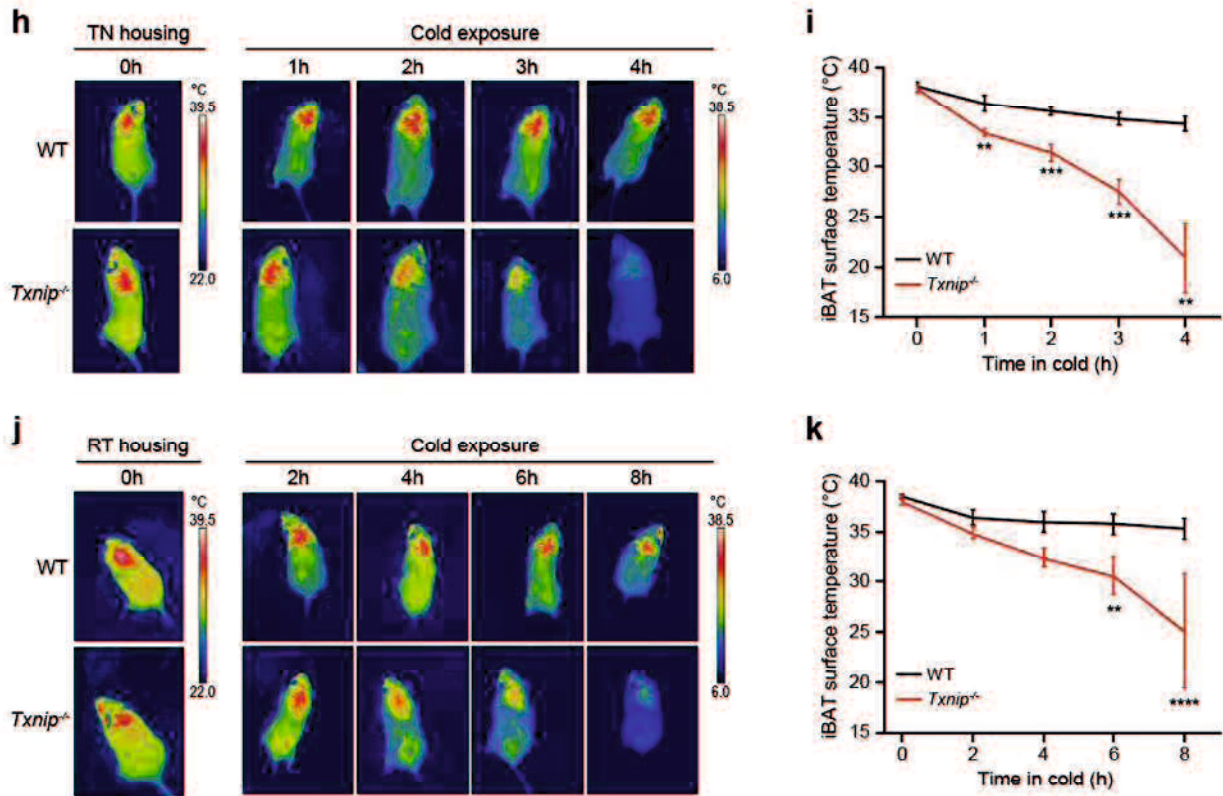


Figure 4. *Txnip*-deficient mice show severe intolerance to acute cold exposure.

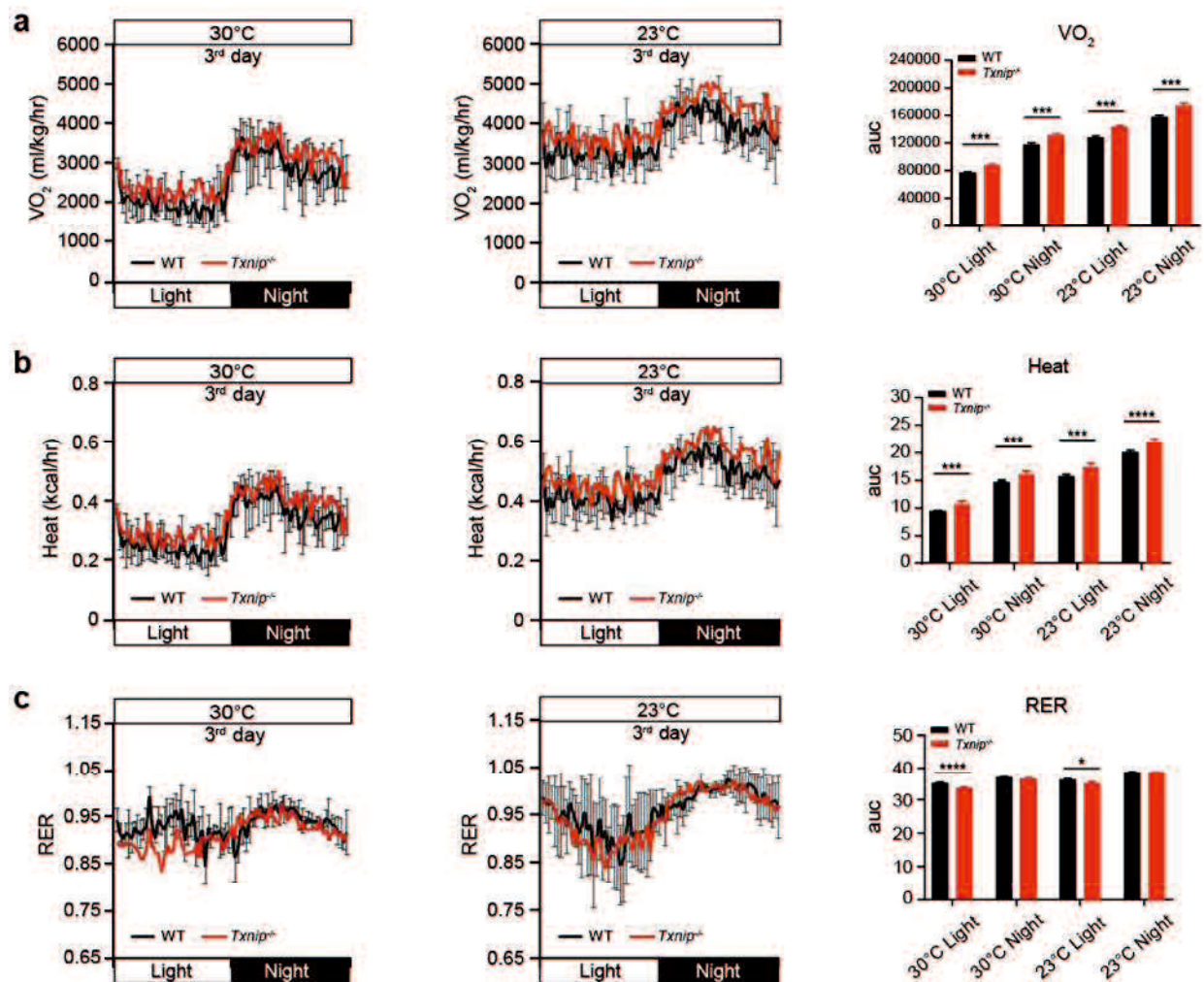
- a)** Western blots and TXNIP quantification in BAT from WT mice housed at TN, RT, and after 6 h cold exposure at 5°C (from RT). α -Tubulin was used as a loading control (n=3 per group);
- b)** Rectal core temperatures of WT, *Txnip*^{+/-}, and *Txnip*^{-/-} mice exposed to acute cold at 5°C after TN acclimation for 1 week (n=10, 8, 10);
- c)** Survival rates of WT, *Txnip*^{+/-}, and *Txnip*^{-/-} mice exposed to acute cold at 5°C after TN acclimation for 1 week (n=18, 15, 18);
- d)** Rectal core body temperature of WT and *Txnip*^{-/-} mice exposed to acute cold at 5°C after pre-housing at RT (n=7);
- e)** Survival rate of WT and *Txnip*^{-/-} mice exposed to acute cold at 5°C after pre-housing at RT (n=10);
- f)** Representative image and H&E staining of interscapular BAT from WT, *Txnip*^{-/-}, and *Txnip*^{-/-} mice exposed to acute cold for 5 h after TN acclimation for 1 week. Scale bar is 50 μ m;
- g)** Representative image and H&E staining of interscapular BAT from WT, *Txnip*^{+/-}, and *Txnip*^{-/-} mice exposed to acute cold for 10 h after pre-housing at RT. Scale bar is 50 μ m;
- h)** Representative infrared images of WT and *Txnip*^{-/-} mice pre-housed in TN, followed by acute cold exposure;
- i)** Interscapular BAT surface temperatures of WT and *Txnip*^{-/-} mice during acute cold exposure after TN acclimation (n=4);
- j)** Representative infrared images of WT and *Txnip*^{-/-} mice pre-housed at RT, followed by acute cold exposure;
- k)** Interscapular BAT surface temperatures of WT and *Txnip*^{-/-} mice during acute cold exposure after pre-housing at RT (n=4).

Data: Mean \pm SD. Statistical analyses: one-way ANOVA with Bonferroni's post-hoc test (**a**), two-way ANOVA with Bonferroni's post-hoc test (**b**, **d**, **i**, **k**), and log-rank (Mantel-Cox) test (**c**, **e**). *p < 0.05, **p < 0.01, ***p < 0.001, and ****p < 0.0001.

5.3 *Txnip* is essential for sustaining adaptive thermogenesis during acute cold stress

Next, we examined the impact of *Txnip* deficiency on thermogenic function by recording whole-body parameters, such as O₂ consumption rate (VO₂), heat generation (Heat), and respiratory exchange ratio (RER). Surprisingly, under both TN and RT conditions, *Txnip*^{-/-} mice exhibited higher VO₂ and Heat than WT mice, while their RER was lower during the light phase (Figure 5a-c). Upon acute transfer to cold conditions following TN acclimation, *Txnip*^{-/-} mice initially

exhibited increased VO_2 and Heat similar to WT mice. However, unlike WT mice, they failed to sustain this respiratory response, experiencing a rapid and profound decline in VO_2 and Heat 1.5 h after transfer to cold conditions (Figure 5d and e). The norepinephrine (NE) challenge in TN-acclimated mice revealed a blunted increase in VO_2 in *Txnip*^{-/-} mice compared to controls (Figure 5f). To gain insights into defective metabolic respiration in *Txnip*^{-/-} mice, we examined mitochondrial abundance and morphology in BAT. A slight but significant decrease in mitochondrial DNA (mtDNA) copy number was detected in BAT of *Txnip*^{-/-} mice under TN conditions, but not at RT (Figure 5g). The ultrastructure of BAT revealed hypertrophic lipid droplets and enlarged mitochondrial size in *Txnip*^{-/-} mice under TN conditions, while mitochondrial cristae length was indistinguishable between genotypes (Figure 5h-j). Subsequently, we assessed sympathetic activation and adrenergic receptor (AR) function in BAT. The NE turnover during cold exposure remained unchanged in BAT of *Txnip*^{-/-} mice (Figure 5k). Regarding AR function, BAT of *Txnip*^{-/-} mice exhibited a significant baseline elevation of phosphorylated hormone-sensitive lipase (pHSL) (Figure 5l and m). Furthermore, the induction of pHSL in *Txnip*^{-/-} BAT by CL316243, a β_3 -AR agonist, mirrored that in WT BAT. These observations implied that sympathetic activation and AR function are preserved in BAT of *Txnip*^{-/-} mice.



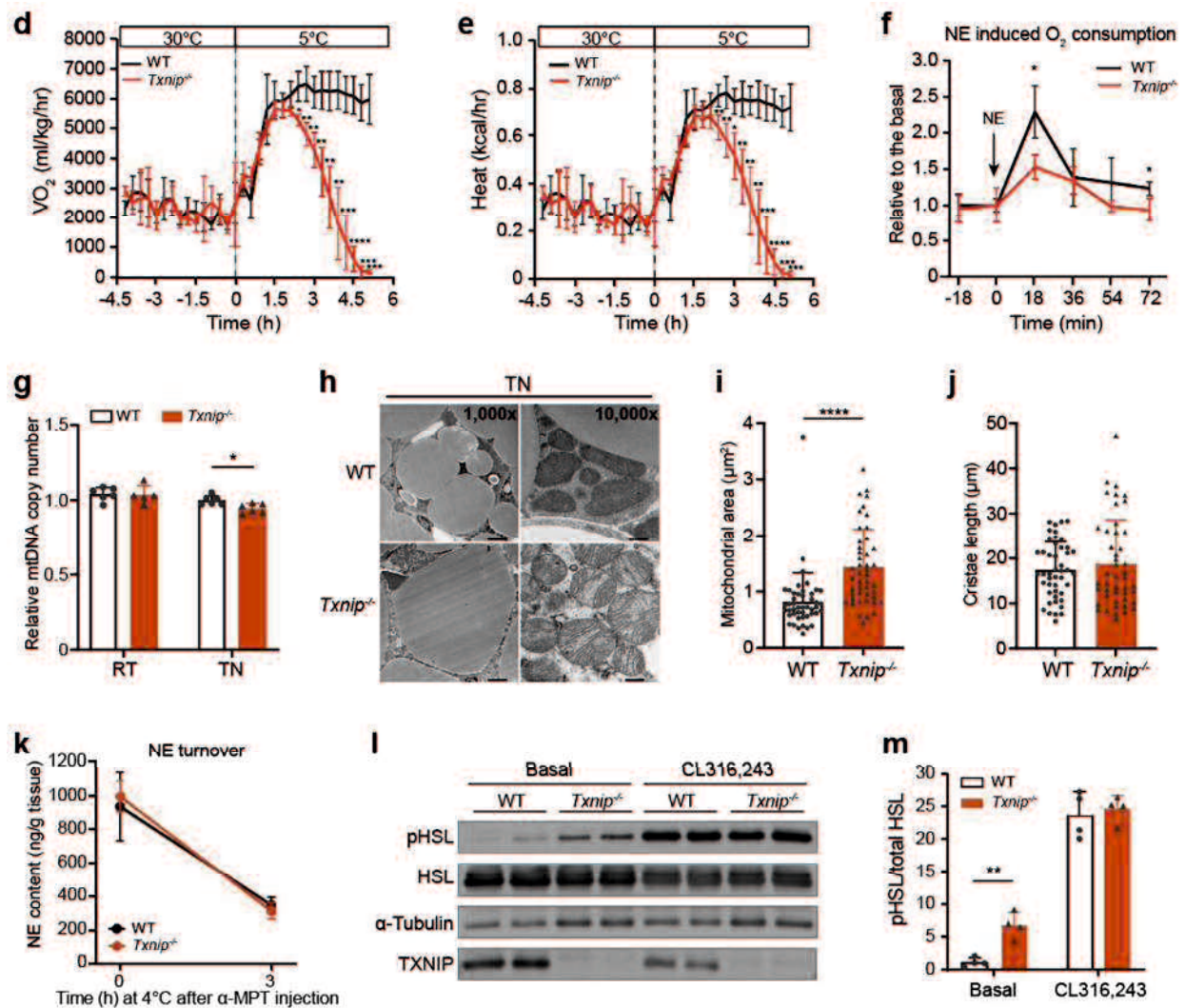


Figure 5. *Txnip* deficiency impairs metabolic respiration in response to acute thermogenic demand.

a, b, c) O_2 consumption rate (VO_2) (**a**), heat production (**b**), and respiratory exchange ratio (RER) (**c**) in WT and *Txnip*^{-/-} mice on the third day of TN and RT housing (n=4);

d, e) VO_2 changes (**d**) and heat production (**e**) in WT and *Txnip*^{-/-} mice transitioning from TN to cold conditions (n=4);

f) Relative VO_2 in TN-acclimated WT and *Txnip*^{-/-} mice post intraperitoneal norepinephrine (NE) injection at 1 mg/kg (body weight) (n=4);

g) Relative mitochondrial DNA copy number in the BAT of WT and *Txnip*^{-/-} mice housed at RT and TN conditions (n=6);

h) Representative TEM images of interscapular BAT from WT and *Txnip*^{-/-} mice acclimated to TN conditions for 1 week. Scale bar is 0.5 μm ;

i, j) Quantification of mitochondrial area (**i**) and total mitochondria cristae length (**j**) in BAT from WT and *Txnip*^{-/-} mice acclimated to TN conditions for 1 week (n=46 mitochondria per group);

k) NE turnover in BAT of WT and *Txnip*^{-/-} mice exposed to acute cold for 3 h after catecholamine synthesis inhibition with α -methyl-p-tyrosine (α -MPT) (200 mg/kg body weight, intraperitoneal injection). The mice were pre-housed at RT (n=6);

l) Western blots of hormone-sensitive lipase (HSL), phosphorylated HSL (pHSL), α -tubulin, and TXNIP in BAT lysates 5 min after injecting β_3 agonist CL316,243 into WT and *Txnip*^{-/-} mice housed at TN conditions (n=4);

m) pHSL quantitation from western blot in (**l**).

Data: Mean \pm SD. Statistical analysis: unpaired Student's t-test (**a-g, i, j, m**), two-way ANOVA with Bonferroni's post-hoc test (**k**). *p < 0.05, **p < 0.01, ***p < 0.001, and ****p < 0.0001.

We further examined the thermogenic capability of *Txnip*^{-/-} mice after acclimating them to 16°C for 7 days, exposing them to chronic mild cold stress. Surprisingly, BAT of *Txnip*^{-/-} mice

exhibited similar morphology to WT BAT, with brown adipocytes displaying multilocular small lipid droplets (Figure 6a and b). With this morphological reversal, *Txnip*^{-/-} mice exhibited similar VO₂ and higher heat generation during mild cold stress (16°C), with a lower RER during the light phase and a higher RER at night, indicating enhanced fuel utilization in *Txnip*^{-/-} mice (Figure 6c-e). Furthermore, *Txnip*^{-/-} mice acclimated to 16°C became resistant to lethal cold stress, showing restored thermogenic response (Figure 6f-i). These results highlight the essential role of *Txnip* in thermogenesis during acute cold stress.

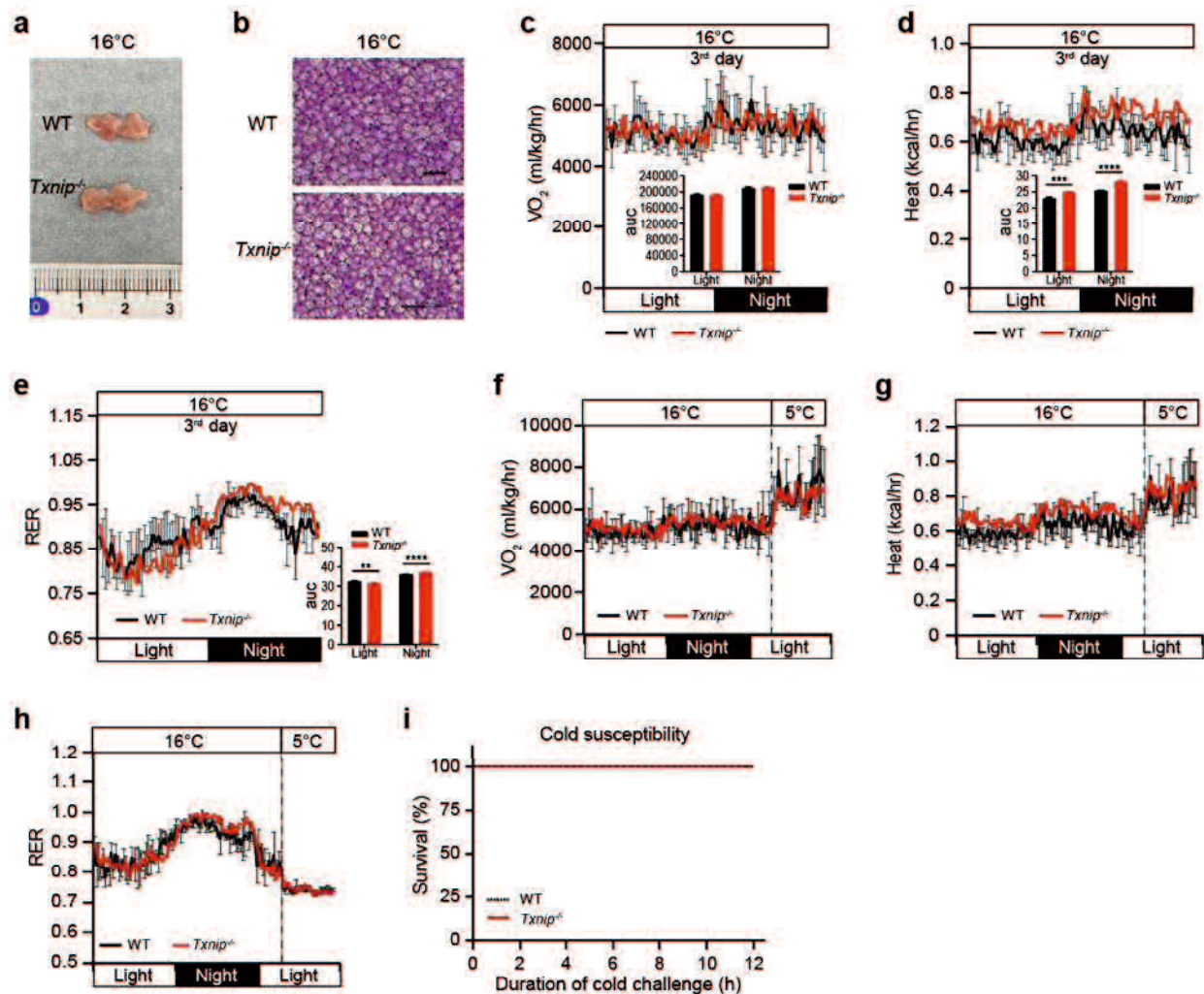


Figure 6. Chronic cold exposure protects *Txnip*^{-/-} mice from lethal hypothermia in cold circumstances
a, b) Representative macroscopic (**a**) and H&E staining (**b**) images of interscapular BAT from WT and *Txnip*^{-/-} mice acclimated to 16°C for 1 week. Scale bar is 50µm;
c-e) VO₂ (**c**), heat production (**d**) and RER (**e**) in WT and *Txnip*^{-/-} mice on the third day of 16°C housing (n=3,4);
f-h) Adaptive changes of VO₂ (**f**), heat production (**g**) and RER (**h**) in WT and *Txnip*^{-/-} mice transitioning from 16°C to cold exposure at 5°C. Mice were exposed to cold for 8 h after pre-housing at 16°C for 1 week (n=3,4);
i) Survival rate of WT and *Txnip*^{-/-} mice exposed to cold after pre-housing at 16°C for 1 week (n=9 per group).
 Data: Mean ± SD. Statistical analysis: unpaired Student's t-test (**c-h**), log-rank (Mantel-Cox) test (**i**). *p < 0.05, **p < 0.01, ***p < 0.001, and ****p < 0.0001.

5.4 *Txnip* maintains basal expression of BAT signature genes

To explore the underlying cause of thermogenic defects, we performed RNA-seq to examine BAT gene expression profiles of *Txnip*^{-/-} mice and their WT littermates housed at RT or TN

conditions. Under RT conditions, 562 genes were dysregulated in *Txnip*^{-/-} mice (291 upregulated and 271 downregulated) (Figure 7a). A more distinct pattern emerged under TN conditions, with 1560 expression changes observed, among which 1111 genes were upregulated and 449 downregulated (Figure 7b). For metabolic genes, *Fabp3* and *Cox8b* displayed significant downregulation among the genes affected at TN conditions, followed by *Dbt*, *Pgc1a*, *Bcat2*, and *Ucp1* (Figure 7b). Interestingly, while *Ucp1*, crucial for canonical thermogenesis, showed downregulation, other genes related to alternative pathways like *Pthr1*, *Ucp2*, and *Ucp3*, exhibited upregulation in *Txnip*^{-/-} BAT. Gene Ontology (GO) analysis of all significantly downregulated genes in *Txnip*^{-/-} BAT revealed prevalent dysregulation in pathways such as branched-chain amino acid (BCAA) degradation, peroxisome, fatty acid oxidation, carboxylic acid catabolic process, mitochondrial membrane, and mitochondrial matrix (Figure 7c and d). Most key genes involved in BAT thermogenesis, lipid metabolism, the tricarboxylic acid (TCA) cycle, and oxidative phosphorylation (OXPHOS) were dysregulated in BAT of *Txnip*^{-/-} mice under both RT and TN conditions (Figure 7e). Notably, these genes showed more pronounced downregulation under TN conditions than at RT (Figure 7e).

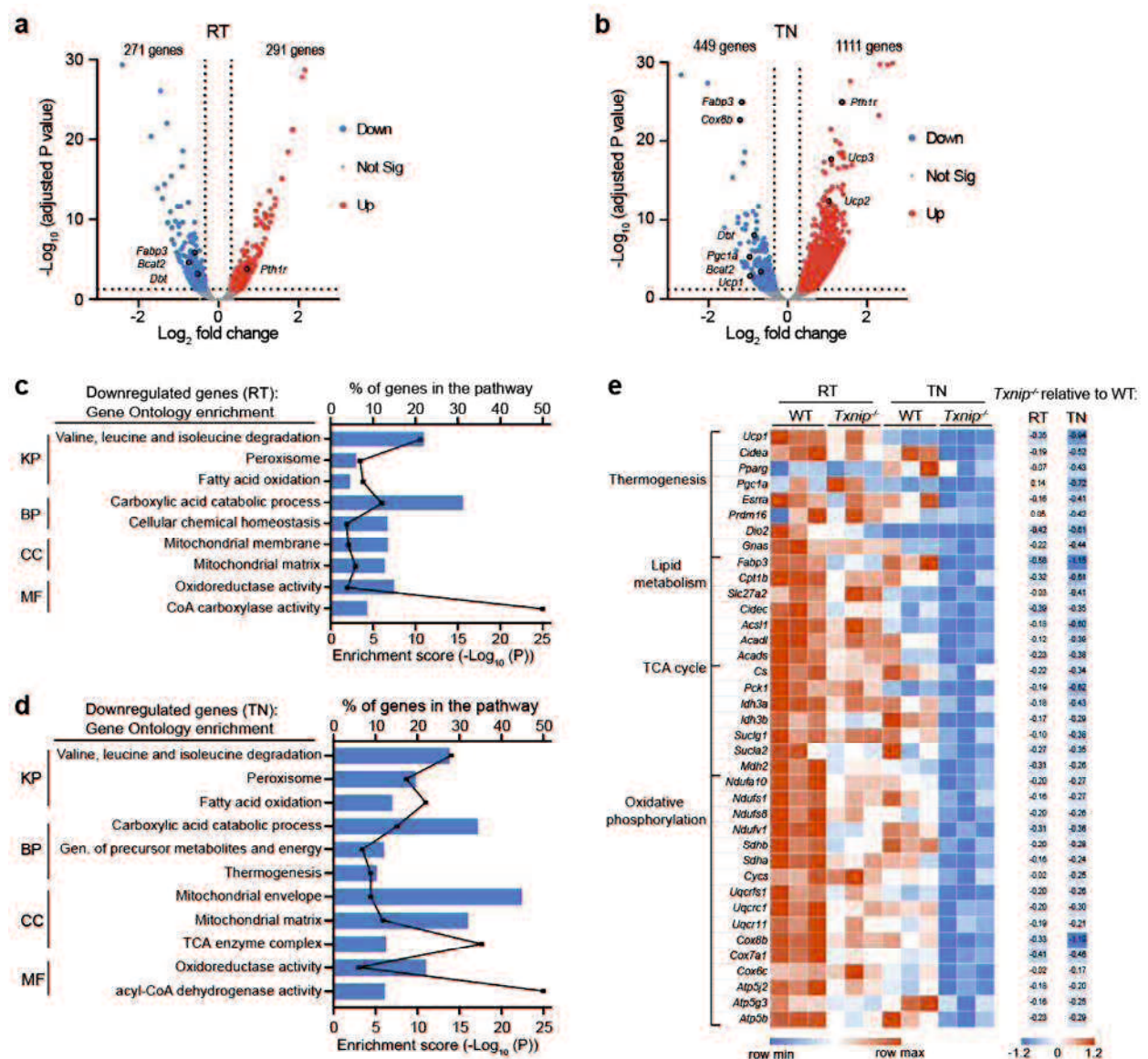
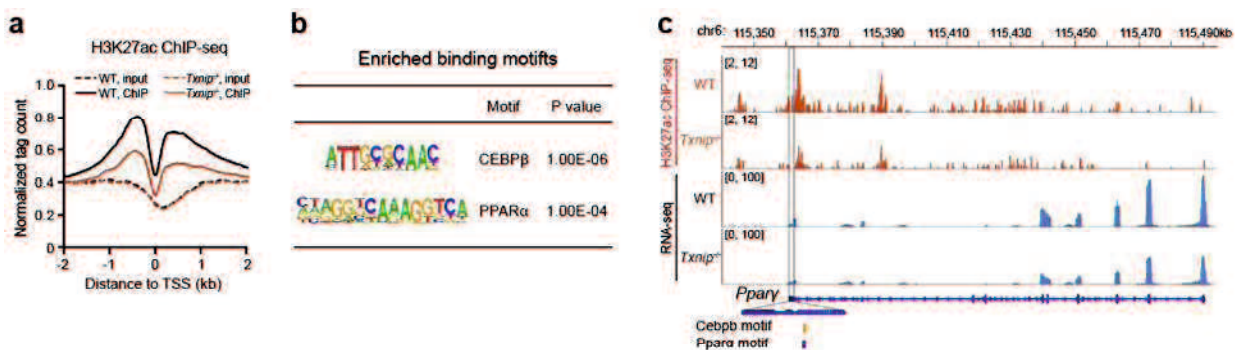


Figure 7. *Txnip* maintains basal thermogenic and metabolic gene expression in BAT.

a, b) Volcano plot of RNA-seq data showing *Txnip*-regulated BAT genes in *Txnip*^{-/-} versus WT mice acclimated to RT (**a**) and TN (**b**) (fold change >1.25 up (red) or <0.8 down (blue)) (n=3);
c, d) Gene Ontology and pathway analysis of downregulated genes in *Txnip*^{-/-} BAT under RT (**c**) and TN (**d**) conditions, identified by RNA-seq and selected based on the enrichment score. The bars represent the enrichment scores for the downregulated pathways. The lines represent the number of downregulated genes as a percentage of the corresponding pathway. (KP, KEGG Pathway; BP, Biological Process; CC, Cellular Component; MF, Molecular Function);
e) Left: Heatmap of selected BAT signature genes in WT and *Txnip*^{-/-} mice housed at RT or TN conditions. Right: Heatmap of selected BAT signature genes in *Txnip*^{-/-} versus WT mice housed at RT or TN conditions.

Despite limited knowledge regarding the role of *Txnip* in transcriptional regulation, we investigated the correlation between transcription profiles and the epigenome within BAT of *Txnip*^{-/-} mice under basal conditions, using chromatin immunoprecipitation followed by sequencing (ChIP-seq) targeting acetylated histone H3 lysine 27 (H3K27ac) as a marker for active enhancers(41). The analysis revealed that the reduced H3K27ac levels in BAT of *Txnip*^{-/-} mice were specifically localized within the proximal regions of the transcription start site (TSS) (Figure 8a). Furthermore, the de novo motif analysis revealed an enrichment of binding motifs associated with known transcription factors, specifically CEBPβ and PPARα within the regions exhibiting decreased H3K27ac levels (Figure 8b). To obtain epigenetic insights into altered thermogenic properties within BAT of *Txnip*^{-/-} mice, we analyzed H3K27ac occupancy on the *Pparγ* loci, a critical regulator of BAT thermogenesis(42). *Txnip* deficiency reduced H3K27ac ChIP signals in the proximal promoter as well as in a distal enhancer, leading to the attenuation of *Pparγ* transcription (Figure 8c). Consistently, *Pgc1α*, a *Pparγ* coactivator, also showed reduced ChIP signals and transcription in *Txnip*^{-/-} BAT under TN conditions (Figure 8d). However, H3K27ac signals in the *Ucp1* loci, the transcription target of *Pparγ* and *Pgc1α*, did not decrease but instead increased in an enhancer region of -2.4 kbp from the TSS in BAT of *Txnip*^{-/-} mice (Figure 8e). Nevertheless, *Ucp1* transcription notably declined, indicating the importance of the paucity of trans-acting factors, such as *Pparγ/α*, *Pgc1α*, and PR/SET Domain 16 (*Prdm16*)(43-45), in suppressing *Ucp1* due to *Txnip* loss. Accordingly, we detected a significant decrease in the protein expression of PPARγ, PGC1α, and UCP1 in BAT of *Txnip*^{-/-} mice under TN conditions (Figure 8f). Additionally, expression of UCP1 and PGC1α remained suppressed in BAT of *Txnip*^{-/-} mice during the acute cold exposure, whereas WAT rather upregulated *Ucp1* with maintaining *Pgc1α* (Figure 8g-k). These findings support a pivotal role for *Txnip* in driving the basal transcription of thermogenic signature genes in BAT.



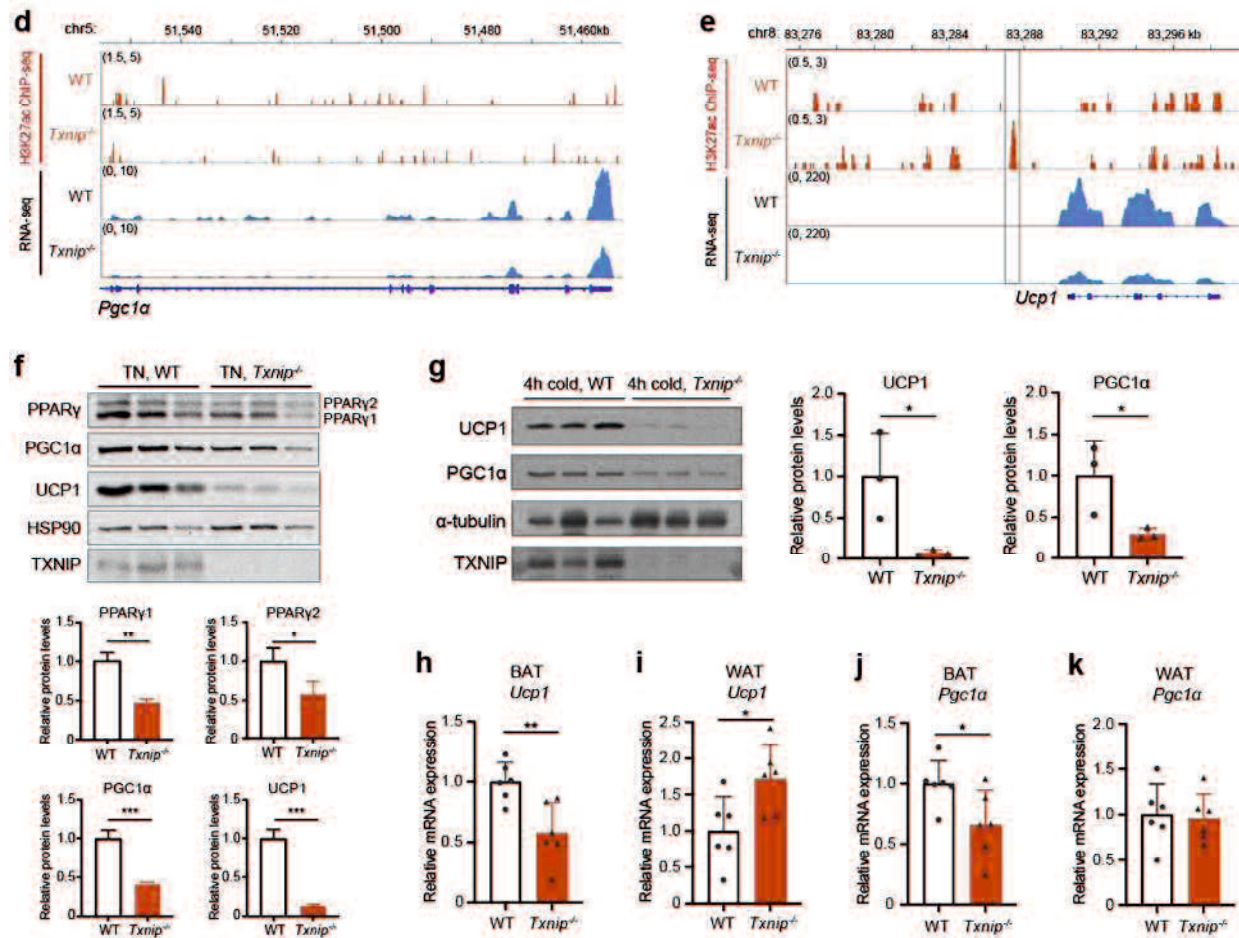


Figure 8. *Txnip* regulates basal thermogenic gene expression in BAT.

a) H3K27ac ChIP-seq profiles within ± 2 kb of the transcription start sites of genes in BAT isolated from WT and *Txnip*^{-/-} mice at TN conditions;

b) Enriched known motifs at sites with decreased H3K27ac binding in BAT from *Txnip*^{-/-} versus WT mice at TN conditions;

c, d, e) Genome browser tracks displaying *Pparγ* loci (**c**) *Pgc1α* loci (**d**) and *Ucp1* loci (**e**) with ChIP-seq and RNA-seq data under TN conditions.

f) Western blots and quantitation of PPAR γ , PGC1 α , and UCP1 in BAT from WT and *Txnip*^{-/-} mice housed at TN conditions. HSP90 was used as the loading control (n=3);

g) Western blots and quantitation of UCP1 and PGC1 α in BAT from WT and *Txnip*^{-/-} mice housed at TN conditions for 1 week, followed by 4-h acute cold exposure at 5°C. α -Tubulin was used as the loading control (n=3).

h, i) *Ucp1* mRNA levels in BAT (**h**) and iWAT (**i**) from WT and *Txnip*^{-/-} mice housed at TN conditions for 1 week, followed by 4-h acute cold exposure at 5°C (n=6);

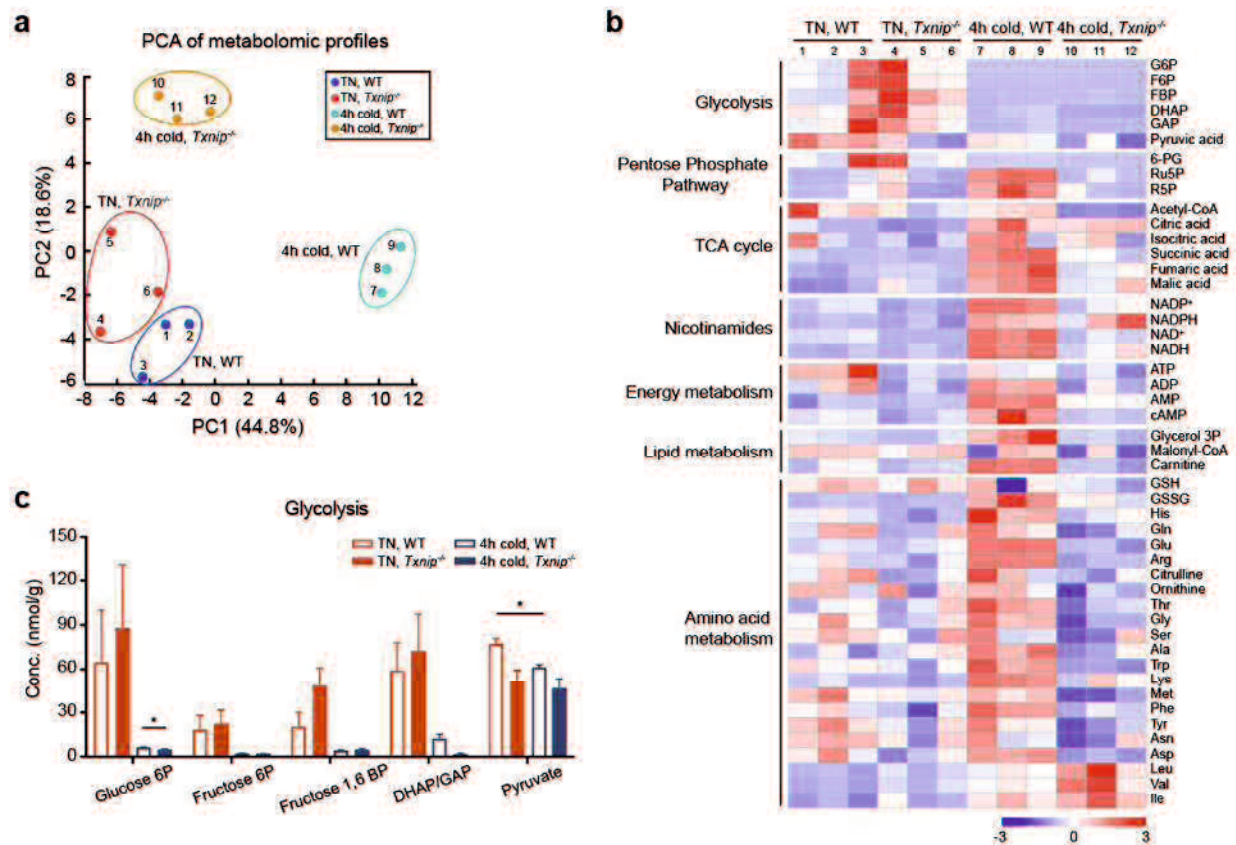
j, k) *Pgc1α* mRNA levels in BAT (**j**) and iWAT (**k**) from WT and *Txnip*^{-/-} mice housed at TN conditions for 1 week, followed by 4-h acute cold exposure at 5°C (n=6)

Data: Mean \pm SD. Statistical analysis: Unpaired Student's t-test (**f-k**). *p < 0.05, **p < 0.01, ***p < 0.001, and ****p < 0.0001.

5.5 *Txnip*-deficient mice fail to activate BAT oxidative metabolism in response to acute cold stress

To investigate the metabolic mechanism underlying blunted thermogenesis due to *Txnip* loss, we analyzed the BAT metabolome in *Txnip*^{-/-} and WT mice acclimated to TN conditions as well as in those exposed to acute cold (5°C, 4 h). The principal component analysis (PCA) showed clear intragroup clustering and notable divergence between *Txnip*^{-/-} and WT BAT, particularly under acute cold stress (Figure 9a). Figure 9b illustrates that in response to acute cold stress,

WT BAT exhibited increased levels of most metabolites related to metabolic pathways and processes other than glycolysis. However, this response was blunted in BAT of *Txnip*^{-/-} mice. In contrast, glycolysis-related metabolites decreased both in WT and *Txnip*^{-/-} BAT during cold stress (Figure 9c). Furthermore, blood glucose levels declined to approximately 100 mg/dL in *Txnip*^{-/-} mice during cold exposure, while remaining steady in WT mice, indicating a potential increase in circulating glucose uptake by *Txnip*^{-/-} mice (Figure 9d). Despite maintaining glycolysis, BAT of *Txnip*^{-/-} mice exhibited a significant decrease in acetyl-CoA under cold exposure compared to WT, suggesting attenuated mobilization of other nutritional substrates (Figure 9e). While WT BAT increased glycerol 3-phosphate (Glycerol 3P) and carnitine levels in response to cold stress, this response was completely abolished in BAT of *Txnip*^{-/-} mice (Figure 9f and g). Considering this observation along with the decreased baseline transcription of lipid metabolism genes (Figure 7e), BAT of *Txnip*^{-/-} mice likely failed to activate fatty acid oxidation (FAO) in response to acute cold stress (Figure 9h). A decline in acetyl-CoA was followed by a significant reduction in the intermediate substrates of the TCA cycle—succinate, fumarate, and malate—along with attenuated baseline transcription of several enzymes involved in this cycle (Figure 9i-l). Importantly, the elevation of NAD⁺, NADH, and the NAD⁺/NADH ratio in response to acute cold stress was abolished in BAT of *Txnip*^{-/-} mice (Figure 9m-o), indicating that BAT of *Txnip*^{-/-} mice failed to activate oxidative metabolism crucial for thermogenesis during acute cold stress.



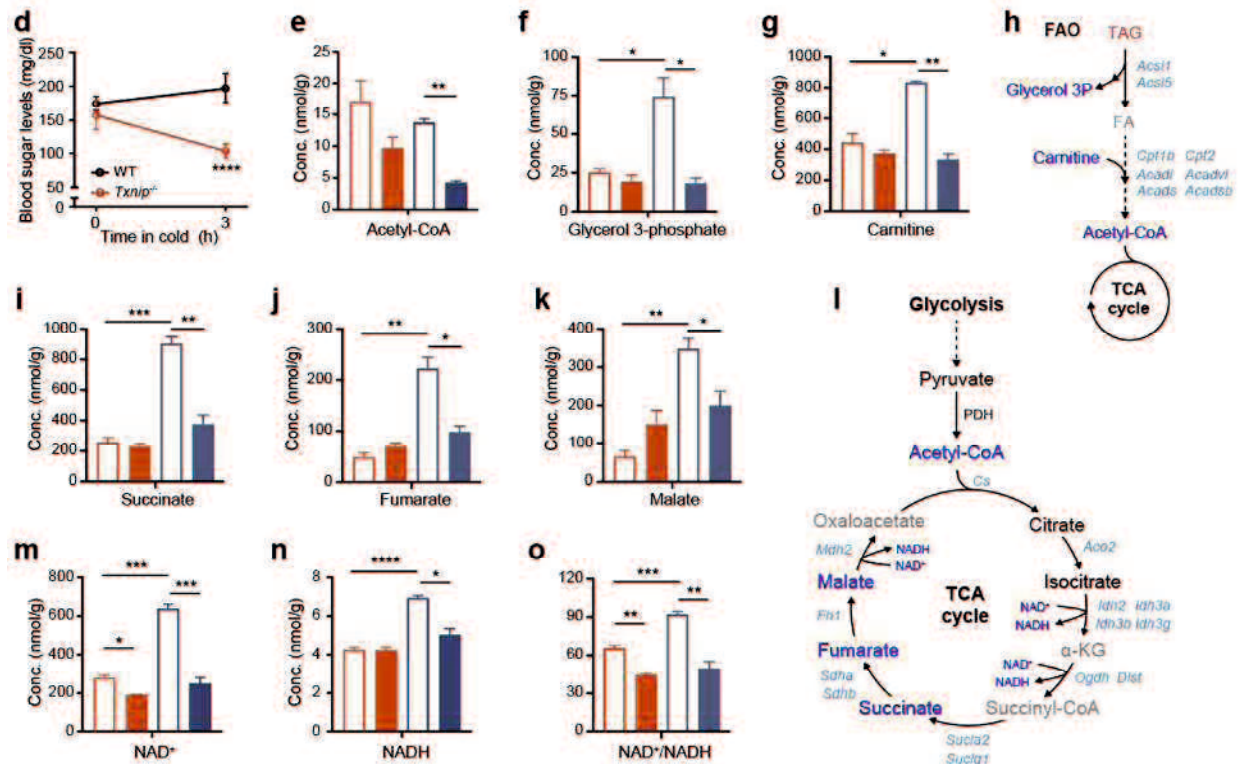


Figure 9. Metabolomic profile alterations in *Txnip*^{-/-} BAT in response to acute cold stress.

a) Principal component analysis (PCA) of the metabolomic data in BAT from WT and *Txnip*^{-/-} mice housed in TN conditions for 1 week, followed by 4-h cold exposure at 5°C (n=3);

b) Heatmap analysis of the selected metabolites in BAT from WT and *Txnip*^{-/-} mice housed at TN conditions for 1 week, followed by 4-h cold exposure at 5°C (n=3);

c) Levels of glycolysis intermediates in BAT of WT and *Txnip*^{-/-} mice housed at TN conditions for 1 week, followed by 4-h cold exposure at 5°C (n=3);

d) Changes in blood sugar levels in WT and *Txnip*^{-/-} mice during acute cold exposure after TN acclimation (n=9);

e-g) Levels of acetyl-CoA (**e**), glycerol 3-phosphate (**f**), and carnitine (**g**) in BAT of WT and *Txnip*^{-/-} mice housed at TN conditions for 1 week, followed by 4-h cold exposure at 5°C (n=3);

h) Changes in fatty acid oxidation (FAO)-related metabolites and genes. Light blue: downregulated genes in *Txnip*^{-/-} versus WT BAT at TN conditions; red: increased metabolite levels in *Txnip*^{-/-} versus WT BAT after 4-h of cold exposure; blue: decreased metabolite levels in *Txnip*^{-/-} versus WT BAT after 4-h of cold exposure; gray: undetectable metabolites.

i-k) Levels of TCA cycle-related organic acids in BAT of WT and *Txnip*^{-/-} mice housed at TN conditions for 1 week, followed by 4-h cold exposure at 5°C (n=3);

l) Changes in TCA cycle-related metabolites and genes. Light blue: downregulated genes in *Txnip*^{-/-} versus WT BAT at TN conditions; blue: decreased metabolite levels in *Txnip*^{-/-} versus WT BAT after 4-h of cold exposure; black: unchanged metabolites between WT and *Txnip*^{-/-} BAT after 4-h of cold exposure; grey: undetectable metabolites.

m-o) Levels of NAD⁺ (**m**), NADH (**n**), NAD⁺/NADH (**o**) in BAT of WT and *Txnip*^{-/-} mice housed at TN conditions for 1 week, followed by 4-h cold exposure at 5°C (n=3).

Data: Mean ± SD (**d**), Mean ± s.e.m. (**c**, **e-g**, **i-k**, **m-o**). Statistical analysis: unpaired Student's t-test (**c**, **e-g**, **i-k**, **m-o**), two-way ANOVA with Bonferroni's post hoc test (**d**). *p < 0.05, **p < 0.01, ***p < 0.001, and ****p < 0.0001.

5.6 *Txnip* deficiency impairs BCAA catabolism in BAT

Amino acids serve as substrates in various metabolic pathways. While most measured amino acids increased in the BAT of WT mice under acute cold stress, this response was blunted in *Txnip*^{-/-} mice (Figure 9b). This was further confirmed by assessing total amino acid levels in BAT (Figure 10a). Interestingly, although no significant change was observed between genotypes under TN acclimation, valine, leucine, and isoleucine levels appeared to increase in

BAT of *Txnip*^{-/-} mice after acute cold exposure (Figure 9b). Their total amounts, measured as branched-chain amino acids (BCAAs), increased approximately 2-fold in *Txnip*^{-/-} mice relative to WT mice after acute cold exposure (Figure 10b). BCAAs are energetically more efficient than other amino acids and are actively catabolized in BAT for thermogenesis during cold exposure(46). We observed that while glutamate levels, generated at the initial step of the BCAA catabolism, markedly increased in WT BAT in response to acute cold stress without a concurrent increase in glutathione (GSH) levels, this response was completely abolished in BAT of *Txnip*^{-/-} mice (Figure 10c and d). Furthermore, the baseline transcription of enzymes and transporters involved in BCAA catabolism was downregulated in BAT of *Txnip*^{-/-} mice (Figure 10e). Thus, these findings indicate the impaired BAT activity in *Txnip*^{-/-} mice to facilitate BCAA catabolism, especially in response to acute thermogenic requirements (Figure 10f). Moreover, while cold-activated BAT promotes systemic BCAA clearance in both humans and mice(46), *Txnip*^{-/-} mice exhibited a progressive increase in circulating BCAA levels during acute cold exposure (Figure 10g and h). This implies a potential attenuation in the clearance of circulating BCAAs associated with their utilization in BAT.

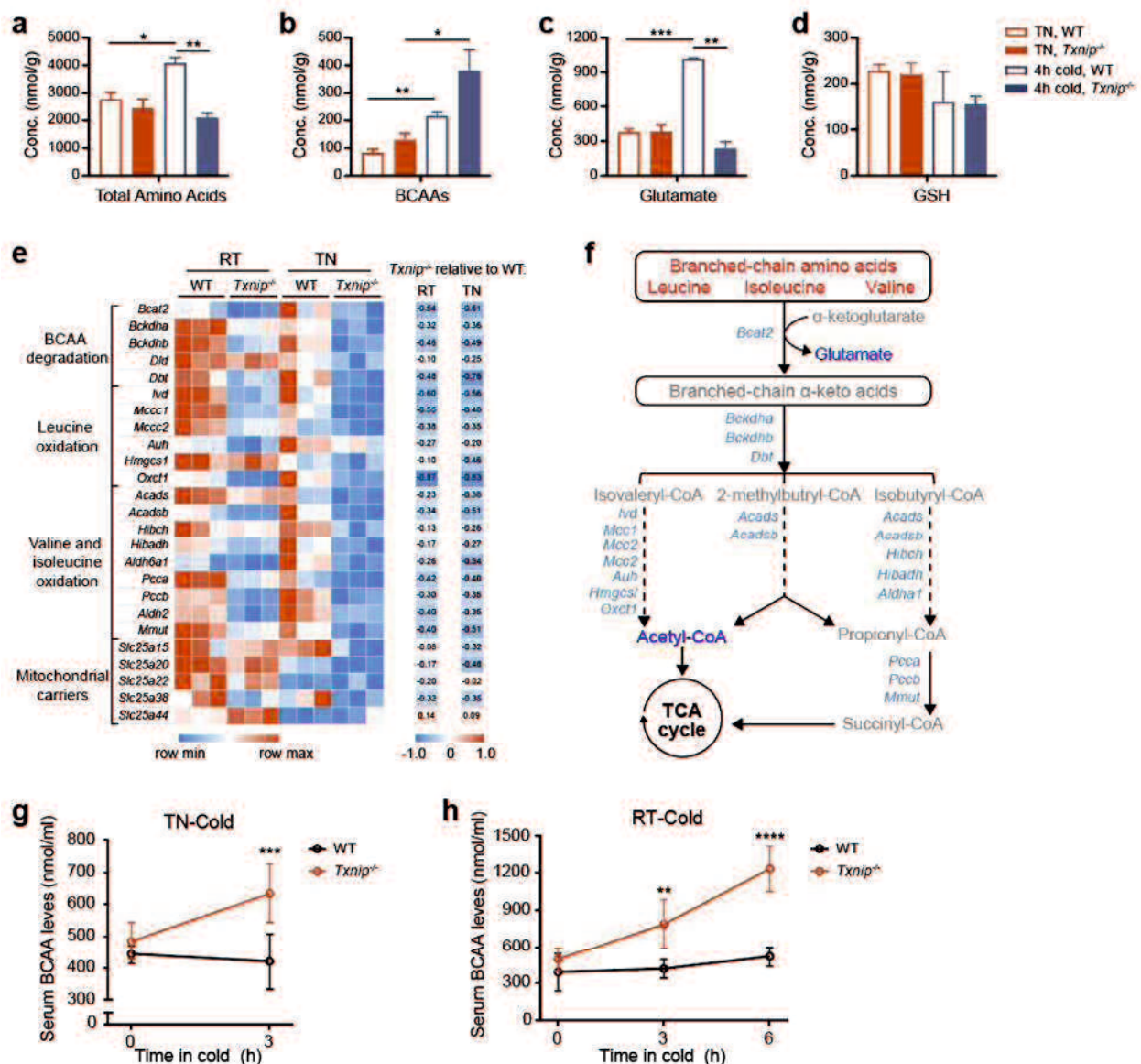


Figure 10. *Txnip* deficiency impairs BAT BCAA catabolism in response to acute cold stress.

a-d) Levels of total Amino acids (a), total BCAAs (b), glutamate (c) and glutathione (GSH) (d) in BAT of TN-acclimated WT and *Txnip*^{-/-} mice for 1 week, followed by 4-h cold exposure at 5°C (n=3);

e) Left: Heatmap of BCAA oxidation genes in BAT from WT and *Txnip*^{-/-} mice housed at RT or TN conditions. Right: Heatmap of BCAA oxidation genes in BAT from *Txnip*^{-/-} mice relative to WT mice housed at RT or TN;

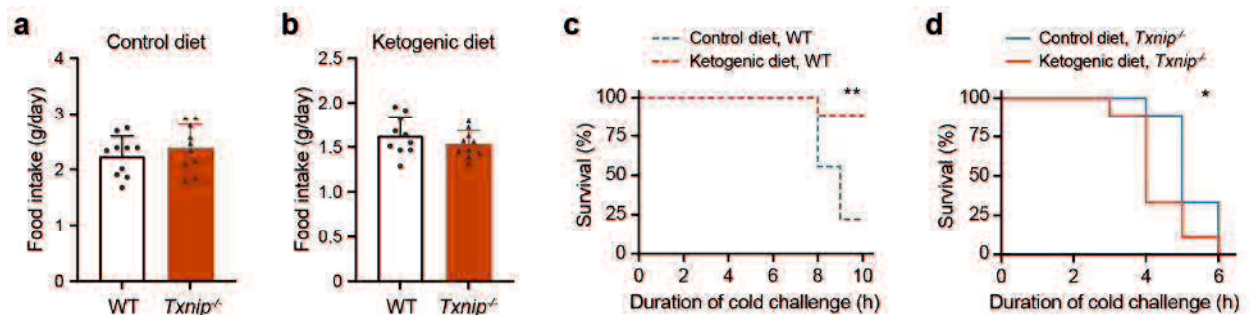
f) Changes in BCAA catabolism-related metabolites and genes. Light blue: downregulated genes in *Txnip*^{-/-} versus WT BAT at TN conditions; red: increased metabolite levels in *Txnip*^{-/-} versus WT BAT after 4-h of cold exposure; blue: decreased metabolite levels in *Txnip*^{-/-} versus WT BAT after 4-h of cold exposure; gray: undetectable metabolites;

g, h) Changes in serum BCAA levels in WT and *Txnip*^{-/-} mice during acute cold exposure after acclimation to TN (g) and RT (h) (n=5 for TN group, n=7, 8 for RT group).

Data: Mean ± s.e.m. (a-d) or mean ± SD (g, h). Statistical analysis: unpaired Student's t-test (a-d), two-way ANOVA with Bonferroni's post-hoc test (g, h). *p < 0.05, **p < 0.01, ***p < 0.001, and ****p < 0.0001.

5.7 A ketogenic diet exacerbates cold intolerance in *Txnip*^{-/-} mice without developing hypoglycemia

A ketogenic diet (KG) stimulates metabolic conditions akin to fasting, inducing a metabolic shift in fuel preference from glucose to fatty acids or ketone bodies. A recent study has shown that a ketogenic diet corrected mitochondrial function in the BAT of a specific mouse line with *Txnip* deficiency(47). Therefore, we tested the effects of a KG on BAT thermogenesis and cold intolerance in *Txnip*^{-/-} mice. Because *Txnip*^{-/-} mice reportedly have susceptibilities to fasting, we used a modified KG in which the carbohydrate proportion was increased to protect the mice (Table 1). Although food intake for the control diet and ketogenic did not differ between WT and *Txnip*^{-/-} mice housed at TN conditions, upon acute cold exposure, WT fed a modified KG significantly improved the survival rate during the observation period (Figure 11a-c). In contrast, despite no hypoglycemic development, *Txnip*^{-/-} mice fed a modified KG died significantly earlier than those fed a control diet (Figure 11d). Consistently with the survival rates, a modified KG slowed a decline in BAT surface temperature during the cold exposure in WT but had the opposite effect in *Txnip*^{-/-} mice (Figure 11e-g). Notably, WT and *Txnip*^{-/-} mice similarly displayed BAT whitening with enlarged unilocular lipid droplets upon TN acclimation with KG feeding (Figure 11h and i). Nevertheless, under the cold stress, the lipid droplets in WT BAT became smaller and morphologically reverted to multilocular, whereas those in BAT of *Txnip*^{-/-} mice showed no distinct changes, indicating its inability to activate utilization of fatty acids for thermogenesis.



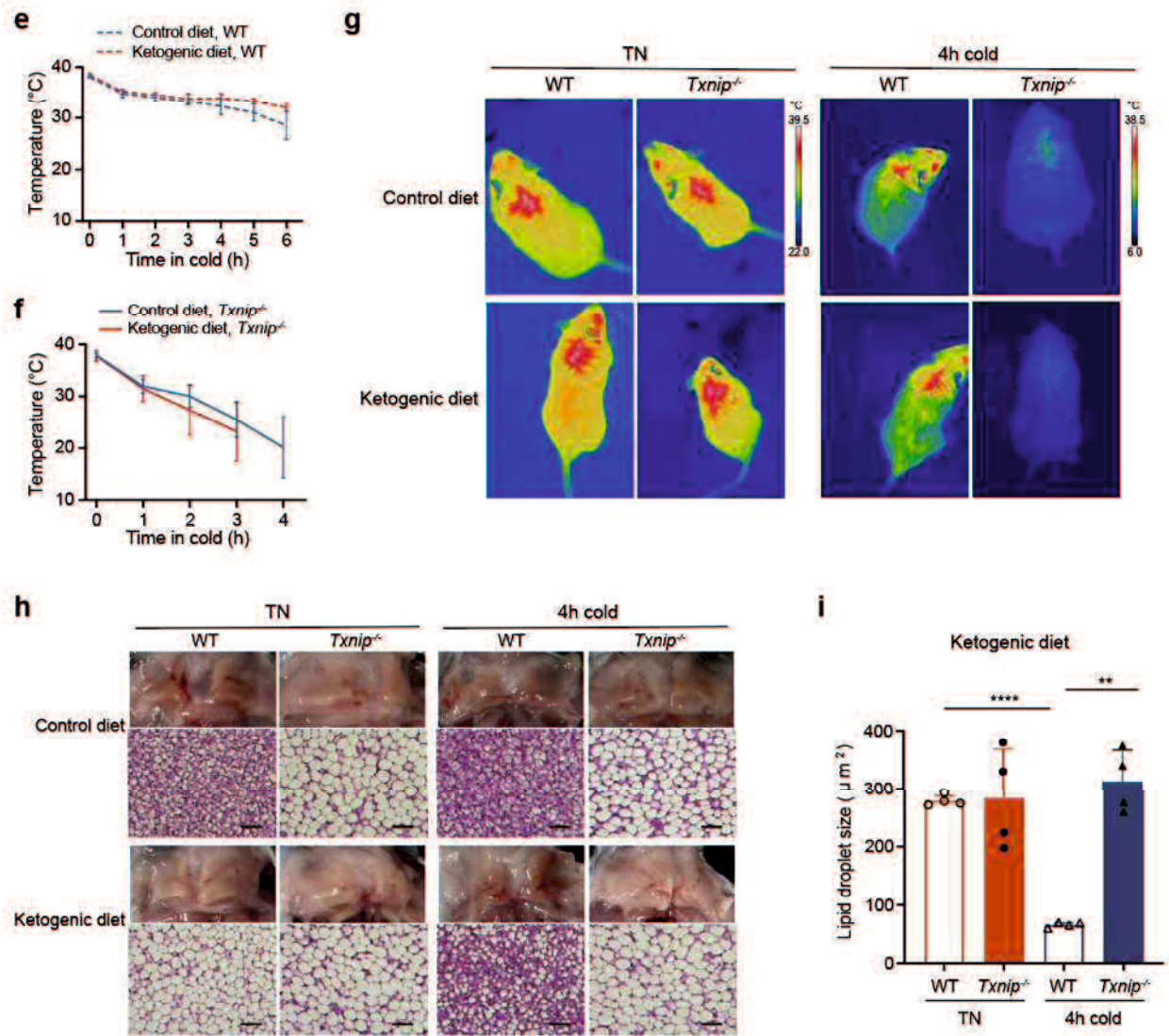


Figure 11. Ketogenic diet fails to restore cold intolerance in *Txnip*^{-/-} mice.

a, b) Food intake for control diet (**a**) and ketogenic diet (**b**) in WT and *Txnip*^{-/-} mice housed at TN conditions (n=10); **c, d**) Survival rates of WT (**c**) and *Txnip*^{-/-} (**d**) mice during acute cold exposure after feeding ketogenic and control diets for 1 week under TN conditions (n=9);

e, f) Interscapular BAT surface temperatures of WT (**e**) and *Txnip*^{-/-} (**f**) mice during acute cold exposure after feeding ketogenic and control diets for 1 week under TN conditions (n=4);

g, h) Representative infrared images (**g**), macroscopic and H&E staining images (**h**) of WT and *Txnip*^{-/-} mice fed a control diet and ketogenic diet for 1 week under TN conditions, followed by 4-h of acute cold exposure;

i) Quantification of lipid droplet size from BAT H&E-stained slides in (**h**) (n=4).

Data: Mean ± SD. Statistical analysis: unpaired Student's t-test (**a, b, i**), log-rank (Mantel–Cox) test (**c, d**), two-way ANOVA with Bonferroni's post-hoc test (**e, f**). *p < 0.05, **p < 0.01, ***p < 0.001, and ****p < 0.0001.

6. Discussion

The tight regulation of metabolic and thermogenic activities is pivotal for maintaining core body temperature in mammals. Although several studies have delved into the transcriptional networks governing thermogenic genes within brown adipocytes, many aspects of this process remain incompletely understood. This study identified *Txnip* as a crucial factor in preserving brown adipocyte identity and ensuring preparedness for acute and life-threatening cold stress. *Txnip*-deficient mice exhibited BAT whitening along with decreased transcription of BAT signature and metabolic genes. Upon exposure to acute cold stress, the BAT of *Txnip*^{-/-} mice failed to activate oxidative metabolism in BCAA and fatty acids, rendering them highly susceptible to severe cold stress. Our findings underscore that *Txnip* plays a role in maintaining BAT identity and is essential for ensuring BAT thermogenic function in response to acute cold stress, providing further insights into inducible thermogenesis under acute cold stress.

The previous studies have indicated that *Txnip*^{-/-} mice are intolerant to starvation, inflammation, and endurance exercise(6, 13, 15), suggesting an integral role of *Txnip* in protection against various physiological stresses. In this context, our study uncovers the impact of reduced *Txnip* expression on thermogenesis, specifically in response to acute cold stress. This finding not only enhances our understanding of mammalian biology but also indicates that *Txnip* plays a crucial role in enabling mice to adapt to environmental changes, potentially supporting their nocturnal activity during evolution.

It has been shown that loss of *Txnip* enhanced insulin secretion and insulin-mediated glucose uptake, facilitating glucose disposal(7, 13). Given the general understanding, whereas the effects of *Txnip*-deficiency on glucose metabolism and BAT function are seemingly contradictory, the recent study that examined the different line of *Txnip*-deficient mice has suggested a possibility that increased glucose influx affects mitochondrial integrity and electron transport chain efficiency in brown adipocytes(47). The metabolomic profile of *Txnip*^{-/-} BAT indicated enhanced glycolysis, similar to WT BAT, in response to acute cold stress. This supposedly accounts for preservation of the early elevation of O₂ consumption rate (VO₂) in *Txnip*^{-/-} mice. However, the mice could not maintain potentiation of metabolic respiration, and their VO₂ rapidly declined. This failure might be attributed to the severely blunted catabolic responses of fatty acids and BCAAs in BAT of *Txnip*^{-/-} mice, hindering its ability to maintain thermogenic metabolism. Starvation, endurance exercise and cold stress, all are the conditions under which mice require *Txnip* for a metabolic shift from glucose to other nutrients. Hence, our observations provide further insights into coordinating fuel selection for adaption to various physiological stresses.

Txnip^{-/-} mice were severely susceptible to acute cold exposure, whereas they were capable of increasing thermogenesis as housing temperatures decreased. This suggests that physiological thermogenic mediators are not critically impaired in *Txnip*^{-/-} mice. In addition, RER recorded in *Txnip*^{-/-} mice significantly decreased during the light phase relative to that recorded in WT, indicating an increase in systemic FA oxidation. Given that thermogenic metabolism in BAT would be blunted by lacking *Txnip*, other thermogenic organs, such as WAT, where FAs are

preferentially utilized, might retain or even potentiate the basal thermogenesis. With a relevance of this observation, WAT showed increased *Ucp1* expression during the acute cold exposure, while this response was eliminated in BAT of *Txnip*^{-/-} mice. Collectively, our observations indicate that Txnip plays a pivotal role in enabling BAT to adaptively activate its thermogenic program when suddenly exposed to life-threatening cold conditions. Although the precise function of Txnip in brown adipocytes remains unclear, a recent report has demonstrated that oxidative function in isolated mitochondria from BAT of a distinct line of *Txnip*-deficient mice was impaired(47). This experimental evidence may, at least partly, explain our observations on BAT. However, to further understand a cell-autonomous role of Txnip in BAT, future studies exploring the effects of brown adipocyte-specific deletion of Txnip will be needed.

Txnip deficiency leads to the downregulation of basal transcription in BAT signature and metabolic genes. We observed a correlation between the downregulation of key regulators, such as *Pparγ* and *Pgc-1α*, critical for BAT thermogenic transcription network and reduced H3K27ac levels on these genes. However, the underlying mechanisms regulated by Txnip remain unclear. A recent report described the nuclear distribution of Txnip in mouse brown adipocytes(48), suggesting a potential nuclear role for Txnip. In addition, the observed upregulation of Txnip in BAT following acute cold exposure raises questions about its increased nuclear expression or facilitated nuclear translocation under cold stress. Consequently, future studies should explore the nuclear function of Txnip in regulating BAT thermogenic gene transcription and its nuclear expression under cold stress.

Intriguingly, in the BAT of *Txnip*^{-/-} mice, the transcription of *Ucp1*, *Pparγ*, and *Pgc-1α* was notably lower at TN conditions than at RT, indicating that the loss of Txnip has a more pronounced effect on the basal expression of these genes than the absence of sympathetic stimulation. This lowered transcription was also observed in several other genes critical for oxidative phosphorylation and FA and BCAA metabolism. Thus, Txnip plays a critical role in maintaining the basal expression of *Ucp1* and other genes regulating oxidative and fuel metabolism in BAT. Our findings underscore the physiological role of Txnip in preserving thermogenesis in response to acute exposure to life-threatening cold temperatures. Txnip plays a unique role in priming brown adipocytes to promptly support thermogenic respiration and immediate heat production. Thus, unlike chronic cold stress-induced thermogenic mechanisms that require time to evolve, Txnip establishes a basal thermogenic tone, enabling BAT to rapidly respond to acute, life-threatening cold exposures.

7. Conclusion

Our study reveals a novel physiological role of Txnip in BAT adaptive thermogenesis in response to acute cold stress. With the involvement of Txnip in various metabolic organs, it emerges as a critical regulator of energy metabolism, adapting to environmental stresses, such as starvation and cold exposure. Therefore, our findings contribute to understanding the physiological basis of responding to acute cold stress and shed light on mammalian biology.

8. Acknowledgement

Throughout my study in the Division of Endocrinology, Metabolism, Hematological Sciences and Therapeutics, Yamaguchi University Graduate School of Medicine, I would like to express my sincere gratitude to all those who have helped me.

First, I would like to express my deepest gratitude to my supervisors, Prof. Tanabe Katsuya and Prof. Tanizawa Yukio (currently President of Yamaguchi University), and my teacher, Dr. Kikuko Amo-Shiinoki for their profound knowledge, excellent guidance, constant encouragement and support in my dissertation work. I am greatly thankful for their kindness, patience, and continuous help throughout the years, not only in my academic studies but also in my daily life. Second, I would like to give my heartfelt thanks to Prof. Ohta Yasuharu, Prof. Okuya Shigeru, and Dr. Taguchi Akihiko for their valuable guidance, suggestions, and technical assistance in my thesis. Also, I am highly grateful to Wada Yukiko and Fujioka Midori for their excellent experimental support, as well as all the other teachers at the Division of Endocrinology, Metabolism, Hematological Sciences and Therapeutics for their direct and indirect help to me. Finally, I am deeply indebted to my family for their endless love and support. Whatever I needed and wherever I went, they were always there to support me without any requirement.

This doctoral dissertation is based on the article "Meng Zou *et al.* Txnip deficiency causes a susceptibility to acute cold stress with brown fat dysfunction in mice," *Journal of Biological Chemistry*, 2024, in press (49).

9. References

1. A. Nishiyama *et al.*, Identification of thioredoxin-binding protein-2/vitamin D(3) up-regulated protein 1 as a negative regulator of thioredoxin function and expression. *J Biol Chem* **274**, 21645-21650 (1999).
2. A. Nishiyama, H. Masutani, H. Nakamura, Y. Nishinaka, J. Yodoi, Redox regulation by thioredoxin and thioredoxin-binding proteins. *IUBMB Life* **52**, 29-33 (2001).
3. E. Junn *et al.*, Vitamin D3 up-regulated protein 1 mediates oxidative stress via suppressing the thioredoxin function. *J Immunol* **164**, 6287-6295 (2000).
4. E. Yoshihara *et al.*, Thioredoxin/Txnip: redoxisome, as a redox switch for the pathogenesis of diseases. *Front Immunol* **4**, 514 (2014).
5. P. Patwari *et al.*, Thioredoxin-independent regulation of metabolism by the alpha-arrestin proteins. *J Biol Chem* **284**, 24996-25003 (2009).
6. R. Zhou, A. Tardivel, B. Thorens, I. Choi, J. Tschopp, Thioredoxin-interacting protein links oxidative stress to inflammasome activation. *Nat Immunol* **11**, 136-140 (2010).
7. N. Wu *et al.*, AMPK-dependent degradation of TXNIP upon energy stress leads to enhanced glucose uptake via GLUT1. *Mol Cell* **49**, 1167-1175 (2013).
8. R. Muraleedharan *et al.*, AMPK-Regulated Astrocytic Lactate Shuttle Plays a Non-Cell-Autonomous Role in Neuronal Survival. *Cell Rep* **32**, 108092 (2020).
9. J. S. Bodnar *et al.*, Positional cloning of the combined hyperlipidemia gene Hyplip1. *Nat Genet* **30**, 110-116 (2002).
10. T. Y. Hui *et al.*, Mice lacking thioredoxin-interacting protein provide evidence linking cellular redox state to appropriate response to nutritional signals. *J Biol Chem* **279**, 24387-24393 (2004).
11. S. S. Sheth *et al.*, Thioredoxin-interacting protein deficiency disrupts the fasting-feeding metabolic transition. *J Lipid Res* **46**, 123-134 (2005).
12. W. A. Chutkow, P. Patwari, J. Yoshioka, R. T. Lee, Thioredoxin-interacting protein (Txnip) is a critical regulator of hepatic glucose production. *J Biol Chem* **283**, 2397-2406 (2008).
13. S. Oka *et al.*, Thioredoxin binding protein-2/thioredoxin-interacting protein is a critical regulator of insulin secretion and peroxisome proliferator-activated receptor function. *Endocrinology* **150**, 1225-1234 (2009).
14. G. Xu, J. Chen, G. Jing, A. Shalev, Thioredoxin-interacting protein regulates insulin transcription through microRNA-204. *Nat Med* **19**, 1141-1146 (2013).
15. K. L. DeBalsi *et al.*, Targeted metabolomics connects thioredoxin-interacting protein (TXNIP) to mitochondrial fuel selection and regulation of specific oxidoreductase enzymes in skeletal muscle. *J Biol Chem* **289**, 8106-8120 (2014).
16. W. A. Chutkow *et al.*, Deletion of the alpha-arrestin protein Txnip in mice promotes adiposity and adipogenesis while preserving insulin sensitivity. *Diabetes* **59**, 1424-1434 (2010).

17. S. Oka *et al.*, Thioredoxin binding protein-2 mediates metabolic adaptation in response to lipopolysaccharide in vivo. *Crit Care Med* **38**, 2345-2351 (2010).
18. E. Yoshihara, TXNIP/TBP-2: A Master Regulator for Glucose Homeostasis. *Antioxidants* **9**, 765 (2020).
19. E. Yoshihara *et al.*, Disruption of TBP-2 ameliorates insulin sensitivity and secretion without affecting obesity. *Nat Commun* **1**, 127 (2010).
20. K. Ikeda, P. Maretich, S. Kajimura, The Common and Distinct Features of Brown and Beige Adipocytes. *Trends in Endocrinology & Metabolism* **29**, 191-200 (2018).
21. S. Kajimura, B. M. Spiegelman, P. Seale, Brown and Beige Fat: Physiological Roles beyond Heat Generation. *Cell Metab* **22**, 546-559 (2015).
22. B. Cannon, J. Nedergaard, Brown adipose tissue: function and physiological significance. *Physiol Rev* **84**, 277-359 (2004).
23. E. T. Chouchani *et al.*, Mitochondrial ROS regulate thermogenic energy expenditure and sulfenylation of UCP1. *Nature* **532**, 112-116 (2016).
24. J. A. Villena *et al.*, Orphan nuclear receptor estrogen-related receptor alpha is essential for adaptive thermogenesis. *Proc Natl Acad Sci U S A* **104**, 1418-1423 (2007).
25. J. Dempersmier *et al.*, Cold-inducible Zfp516 activates UCP1 transcription to promote browning of white fat and development of brown fat. *Mol Cell* **57**, 235-246 (2015).
26. A. Loft, I. Forss, S. Mandrup, Genome-Wide Insights into the Development and Function of Thermogenic Adipocytes. *Trends Endocrinol Metab* **28**, 104-120 (2017).
27. M. J. Emmett *et al.*, Histone deacetylase 3 prepares brown adipose tissue for acute thermogenic challenge. *Nature* **546**, 544-548 (2017).
28. M. Ahmadian *et al.*, ERR γ Preserves Brown Fat Innate Thermogenic Activity. *Cell Rep* **22**, 2849-2859 (2018).
29. S. Oka *et al.*, Impaired fatty acid utilization in thioredoxin binding protein-2 (TBP-2)-deficient mice: a unique animal model of Reye syndrome. *Faseb j* **20**, 121-123 (2006).
30. J. Folch, M. Lees, G. H. Sloane Stanley, A simple method for the isolation and purification of total lipides from animal tissues. *J Biol Chem* **226**, 497-509 (1957).
31. S. Spector, A. Sjoerdsma, S. Udenfriend, BLOCKADE OF ENDOGENOUS NOREPINEPHRINE SYNTHESIS BY ALPHA-METHYL-TYROSINE, AN INHIBITOR OF TYROSINE HYDROXYLASE. *J Pharmacol Exp Ther* **147**, 86-95 (1965).
32. A. Dobin *et al.*, STAR: ultrafast universal RNA-seq aligner. *Bioinformatics* **29**, 15-21 (2013).
33. S. Heinz *et al.*, Simple combinations of lineage-determining transcription factors prime cis-regulatory elements required for macrophage and B cell identities. *Mol Cell* **38**, 576-589 (2010).
34. M. I. Love, W. Huber, S. Anders, Moderated estimation of fold change and dispersion for RNA-seq data with DESeq2. *Genome Biol* **15**, 550 (2014).
35. B. Langmead, S. L. Salzberg, Fast gapped-read alignment with Bowtie 2. *Nat Methods*

- 9, 357-359 (2012).
36. Y. Ohashi *et al.*, Depiction of metabolome changes in histidine-starved *Escherichia coli* by CE-TOFMS. *Mol Biosyst* **4**, 135-147 (2008).
 37. T. Ooga *et al.*, Metabolomic anatomy of an animal model revealing homeostatic imbalances in dyslipidaemia. *Mol Biosyst* **7**, 1217-1223 (2011).
 38. M. Sugimoto, D. T. Wong, A. Hirayama, T. Soga, M. Tomita, Capillary electrophoresis mass spectrometry-based saliva metabolomics identified oral, breast and pancreatic cancer-specific profiles. *Metabolomics* **6**, 78-95 (2010).
 39. H. Yamamoto *et al.*, Statistical hypothesis testing of factor loading in principal component analysis and its application to metabolite set enrichment analysis. *BMC Bioinformatics* **15**, 51 (2014).
 40. B. H. Junker, C. Klukas, F. Schreiber, VANTED: a system for advanced data analysis and visualization in the context of biological networks. *BMC Bioinformatics* **7**, 109 (2006).
 41. A. Rada-Iglesias *et al.*, A unique chromatin signature uncovers early developmental enhancers in humans. *Nature* **470**, 279-283 (2011).
 42. M. K. Ramlee *et al.*, Histone H3 K27 acetylation marks a potent enhancer element on the adipogenic master regulator gene *Pparg2*. *Cell Cycle* **13**, 3414-3422 (2014).
 43. M. J. Barbera *et al.*, Peroxisome proliferator-activated receptor alpha activates transcription of the brown fat uncoupling protein-1 gene. A link between regulation of the thermogenic and lipid oxidation pathways in the brown fat cell. *J Biol Chem* **276**, 1486-1493 (2001).
 44. M. J. Harms *et al.*, PRDM16 binds MED1 and controls chromatin architecture to determine a brown fat transcriptional program. *Genes Dev* **29**, 298-307 (2015).
 45. S. Iida, W. Chen, T. Nakadai, Y. Ohkuma, R. G. Roeder, PRDM16 enhances nuclear receptor-dependent transcription of the brown fat-specific *Ucp1* gene through interactions with Mediator subunit MED1. *Genes Dev* **29**, 308-321 (2015).
 46. T. Yoneshiro *et al.*, BCAA catabolism in brown fat controls energy homeostasis through SLC25A44. *Nature* **572**, 614-619 (2019).
 47. A. N. Waldhart *et al.*, Excess dietary carbohydrate affects mitochondrial integrity as observed in brown adipose tissue. *Cell Rep* **36**, 109488 (2021).
 48. A. N. Waldhart, K. H. Lau, H. Dykstra, T. Avequin, N. Wu, Optimal HSF1 activation in response to acute cold stress in BAT requires nuclear TXNIP. *iScience* **26**, 106538 (2023).
 49. M. Zou *et al.*, *Txnip* deficiency causes susceptibility to acute cold stress with brown fat dysfunction in mice. *Journal of Biological Chemistry*, in press (2024).